FISEVIER

Contents lists available at ScienceDirect

Journal of Hydrology

journal homepage: www.elsevier.com/locate/jhydrol



Research papers

Indications of preferential groundwater seepage feeding northern peatland pools

Henry E. Moore a,*, Xavier Comas b, Martin A. Briggs c, Andrew S. Reeved, Lee D. Slater a,e

- a Ruigers University Newark, Department of Earth, and Environmental Sciences, 101 Warren St. Smith Hall Room 135 Newark, NJ 07102, United States
- ^b Florida Atlantic University, Department of Geosciences, 777 Glades Road, Boca Raton, FL 33431, United States
- c U.S. Geological Survey, Observing Systems Division, Hydrologic Remote Sensing Branch, 11 Sherman Place, Unit 5015, Storrs, CT 06269, United States
- d University of Maine, School of Earth and Climate Sciences, 5790 Bryand Global Sciences Center, Orono, ME 04469-5790, United States
- e Pacific Northwest National Laboratory, 902 Battle Blvd, Richland, WA 99354, United States

ARTICLE INFO

Keywords: Peatland pools Groundwater Hydrogeophysics Temperature Ground-penetrating radar Upwelling

ABSTRACT

Groundwater seepage from underlying permeable glacial sedimentary structures, such as eskers, has been hypothesized to directly feed pools in northern peat bogs. These hypotheses directly contradict classical peat bog models for ombrogenous systems, wherein meteoric water is the sole water input to these systems. Variations in the underlying mineral sediment in contact with the peat imply that unrecognized hydrogeologic connectivity may exist with pools in northern peat bogs, particularly where high permeability materials are in contact with the peat. Seepage dynamics originating from these structural variations were investigated using a suite of thermal and hydrogeophysical methods deployed around pools in a peat bog of northeastern Maine, USA. Thermal characterization methods mapped anomalies that were confirmed as matrix seepage or preferential flow pathways (PFPs). Geochemical methods were employed at identified thermal anomalies to confirm upwelling of solute-rich groundwater. Conduits around pools were associated with surficial terminations of suspected peat pipes, based on the inference of pathways extending down into the peat, that focus flow through PFPs in the peat matrix. Discharge also occurred through the peat matrix adjacent to suspected pipe structures and matrix seepage rates were quantified using analysis of diurnal temperature signals recorded at multiple depths. Seepage rates, with a maximum of nearly 0.4 m/d, were measured at localized points around pools. Periods of synchronized temperatures paired with highly muted diurnal temperature signals, recorded in diurnal temperature with depth data, were interpreted qualitatively as activation of strong upward discharge rates through suspected peat pipes. These time periods correlated strongly with local precipitation events around the peatland. Ground-penetrating radar surveys revealed discontinuities in the low permeability glacio-marine clay at the mineral sediment-peat interface, interpreted to be regional glacial esker deposits, which were located beneath and around pools. Heat tracing, specific conductance contrasts, seepage rates, and trace metal concentrations all imply groundwater seepage originating from underlying permeable glacial esker deposits and directly sourcing pools. Preferential groundwater inputs into northern peat bogs may play a key role in developing and maintaining pool systems, with enhanced solute transport impacting peatland ecology, water resources, and carbon cycling.

1. Introduction

Northern peatlands are wetland systems that locally dominate carbon-cycling in the critical zone, defined as the near-surface of the Earth that extends from the upper extent of bedrock, through the soil matrix, and to the top of the vegetation canopy (Giardino and Houser, 2015). These systems are classified into two distinct types based on the water supplied to them, with fens supplied by minerogenous waters and

bogs supplied by ombrogenous waters (Rydin et al., 2013). The traditional conceptual hydrologic model of natural ombrogenous peat bogs is based on precipitation input into a basin that is hydrologically isolated by a low permeability stratigraphic layer and the domed structure (Weber, 1902; Weber, 1908; Bragg, 2002). This conceptual model does not consider the role of discrete sediment permeability variation along the base of the peat bog in regulating hydrology and groundwater connectivity. Peat accumulation, bog growth, bog structure, and

^{*} Corresponding author at: Department of Earth and Environmental Sciences, 101 Warren Street Smith Hall 135, Newark, NJ 07102, United States. E-mail address: hem62@rutgers.edu (H.E. Moore).

methane gas accumulation/sequestration have been modeled to depend upon this hydrologically isolated conceptual model (Clymo, 1984). However, evidence for exchanges between groundwater (i.e., water originating from local shallow aquifers) and peat pore water exists in hydrological and geophysical datasets (Reeve et al., 2000; Reeve et al., 2001; Bendell-Young, 2003; Comas et al., 2004; Reeve et al., 2006; Reeve et al., 2009). Vertical groundwater upwelling into peat bogs may support the biodiversity of unique ecologic subsystems that benefit from temperature and nutrient regimes established by upwelling at the surface. Unrecognized groundwater inputs to bogs may substantially affect the water balance of the system. Such inputs could have implications for bog resilience to drying from anthropogenic climate change. Furthermore, groundwater upwelling may promote carbon cycling, with upwelling driving carbon gas ebullition to the surface or downwelling enhancing labile carbon concentrations in the peat matrix (Chanton et al., 1995; Hribljan et al., 2014; Chen et al., 2020). Geophysical studies, paired with hydrological models, provide evidence of vertical flow occurring adjacent to underlying permeable esker deposits in an undisturbed peat bog (Comas et al., 2004). Paired hydrological models show that flow cells of peat pore water, cyclical flow patterns driving vertical flow, develop based on two primary drivers in peatlands: 1) the topography changes in the peatland basin and 2) the permeability contrast between the peat matrix and the underlying mineral sediments (Reeve et al., 2000; Reeve et al., 2009). The evolution in the conceptual hydrostratigraphy of peat bogs pits negligible flow of peat pore water in the peat matrix against a more dynamic flow regime as shown in the flow-cell model (Fig. 1; Reeve et al., 2009).

Additionally, geophysical imaging beneath peat bogs, confirmed by coring, has identified the presence of permeable mineral deposits in contact with the base of the bogs beneath surficial pool locations (Comas et al., 2004; Comas et al., 2005; Comas et al., 2011; Chen et al., 2020). Underlying glacial esker ridges have further been inferred to influence pool formation and vegetation gradients (Comas et al., 2004; Comas et al., 2005; Comas et al., 2011). Hydrogeophysical studies also show evidence of upwelling in peat deposits along a riparian corridor, with variations in the underlying mineral sediment slope inferred to enhance the formation of springs and pools at the surface (Lowry et al., 2009; Hare et al., 2017). Analysis of surface water chemistry has further suggested that inputs of mineral-enhanced groundwater feed pools, with elevated levels of iron and manganese trace elements identified as key

indicators (Bendell-Young, 2003). Hydraulic head measurements and pore water chemistry data also provide evidence for vertical downward flow towards underlying permeable esker deposits (Reeve et al., 2009; Chen et al., 2020).

Despite previous hydrogeophysical observations, the nature of the hydrologic connectivity between underlying permeable mineral sediments and the surface of undisturbed peat bogs remains poorly understood. However, some observations support the connectivity occurring through preferential flow via pipes in peat bogs. Horizontal peat pipes, tube-like void geometries serving as preferential flow pathways for peat pore water within the peat matrix, are well documented throughout northern peat bogs (Holden and Burt, 2002). Mapping of these peat pipes using geophysical techniques shows lateral hydrologic connectivity within a peat bog (Holden et al., 2002), as pipes channel water and transport nutrients laterally within the basins (Woo and DiCenzo, 1988; Holden and Burt, 2002; Baird et al., 2009; Hill, 2012; Kline, 2014). However, evidence for the vertical hydrologic connectivity between high permeability lenses and the bog surface that may be associated with peat piping, or other vertical preferential flow pathways, has not been investigated in undisturbed northern peatland pool settings.

Highly localized preferential flow was found to occur at point sources within an anthropogenically modified cranberry peat bog overlying unconfined, permeable glacial sediments (Hare et al., 2017). Evidence for peat pipe-driven upwards vertical flow was identified using thermal characterization methods, which included estimates of vertical fluxes at the surface associated with both matrix seepage and pipe-driven groundwater seepage (Hare et al., 2017). This work shows, through a wealth of evidence, that peat piping is directly connected to the local shallow aguifer. These connections are controlled, in part, by changes in the slope of sandy mineral sediments (Hare et al., 2017). These preferential flow pathways were also shown to feed surface water channels in this cranberry bog (Hare et al., 2017), as was indicated by earlier work (Lowry et al., 2009). These observations highlight the need to investigate the possibility of preferential exchange impacting the hydrology of natural peat bog systems where the extent of permeable mineral soil deposits is more spatially constrained.

In this study, we seek evidence for preferential upwelling of groundwater originating from discrete permeable glacial deposits, embedded in otherwise low-permeability deposits, and terminating around peatland pools, hereafter referred to as pools for brevity, in a

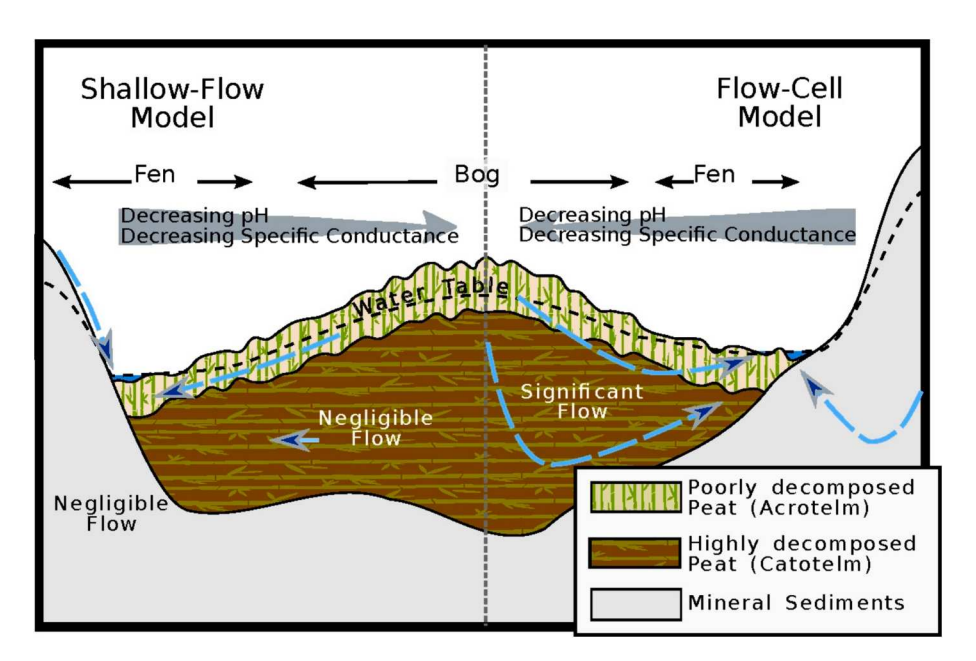


Fig. 1. Traditional shallow-flow model of ombrotrophic raised peat bogs versus the contemporary flow-cell model developed in recent hydrological studies (i.e. Reeve et al., 2000; Reeve et al., 2009).

northern peat bog. Permeable glacial deposits are hypothesized to source groundwater to pools via preferential piping through the peat matrix. A multi-scale hydrogeophysical methodology was employed to investigate zones of preferential groundwater upwelling. Using a combination of heat tracing, aqueous geochemistry, and near-surface geophysical methods, we find evidence for matrix seepage and preferential flowpaths of groundwater feeding pools. Our results indicate a strong association between surficial upwelling zones feeding pools and underlying permeable esker deposits. This study reveals multiparameter evidence for the role of discrete glacial sediment permeability variations on vertical groundwater exchange with the overlying peat matrix and seepage to the surface proximal to pools.

2. MATERIAL AND METHODS

2.1. Study area and approach

The northern peat bog of Sawtelle Heath, located in Washington County, Maine USA, was selected to examine the influences of underlying permeable mineral sediments on pools based on the proximity to surficial esker deposits and visible pool patterning (Fig. 2). Bedrock beneath the peat bog has been mapped as the Silurian Flume Ridge Formation, an interbedded calcareous siltstone-slate unit containing quartzofeldspathic wackes within a chlorite metamorphic zone (Ludman, 1990; Ludman and Hill, 1990; West et al., 1992). Numerous

structural geological complexities are mapped in exposed bedrock outcrops surrounding Sawtelle Heath (Ludman, 1990; Ludman and Hill, 1990). The Pocomoonshine Mountain Fault Zone is located to the north, with Sawtelle Heath sitting atop the upthrown block of the oblique strike-slip fault (Ludman, 1990; Ludman and Hill, 1990). The Silurian Flume Ridge Formation and associated bedrock structural geology are overlaid by regional glacial deposits (Osberg et al., 1985; Comas et al., 2005). With the regional recession of glaciers during the late Pleistocene epoch, sediments of esker systems were deposited (Shreve, 1985; Comas et al., 2005). These eskers are visible on the landscape as sharp ridges of poorly sorted sands and gravels that are visibly adjacent to many peatlands of northeastern Maine and have been shown to extend beneath peat deposits (Shreve, 1985; Comas et al., 2005). Prior to field investigation, surficial esker deposits were identified along the eastern border of Sawtelle Heath (Fig. 2) using digital elevation models (DEMs; Maine Geological Survey, 2016), in QGIS (QGIS.org, 2022) software (Comas et al., 2021). A marine transgression occurred simultaneously with the regional deglaciation event in the late Pleistocene epoch that deposited the Presumpscot Formation over the regional glacial deposits (Fig. 2). The Presumpscot Formation is a glacio-marine silt-clay that generally serves as the low permeability layer controlling the development of peatlands in Maine within the marine limit (Osberg et al., 1985). As deglaciation continued regionally, isostatic rebound of the landscape of Maine resulted in a marine regression, ending the deposition of the Presumpscot Formation (Borns et al., 1963). Regional drainage patterns

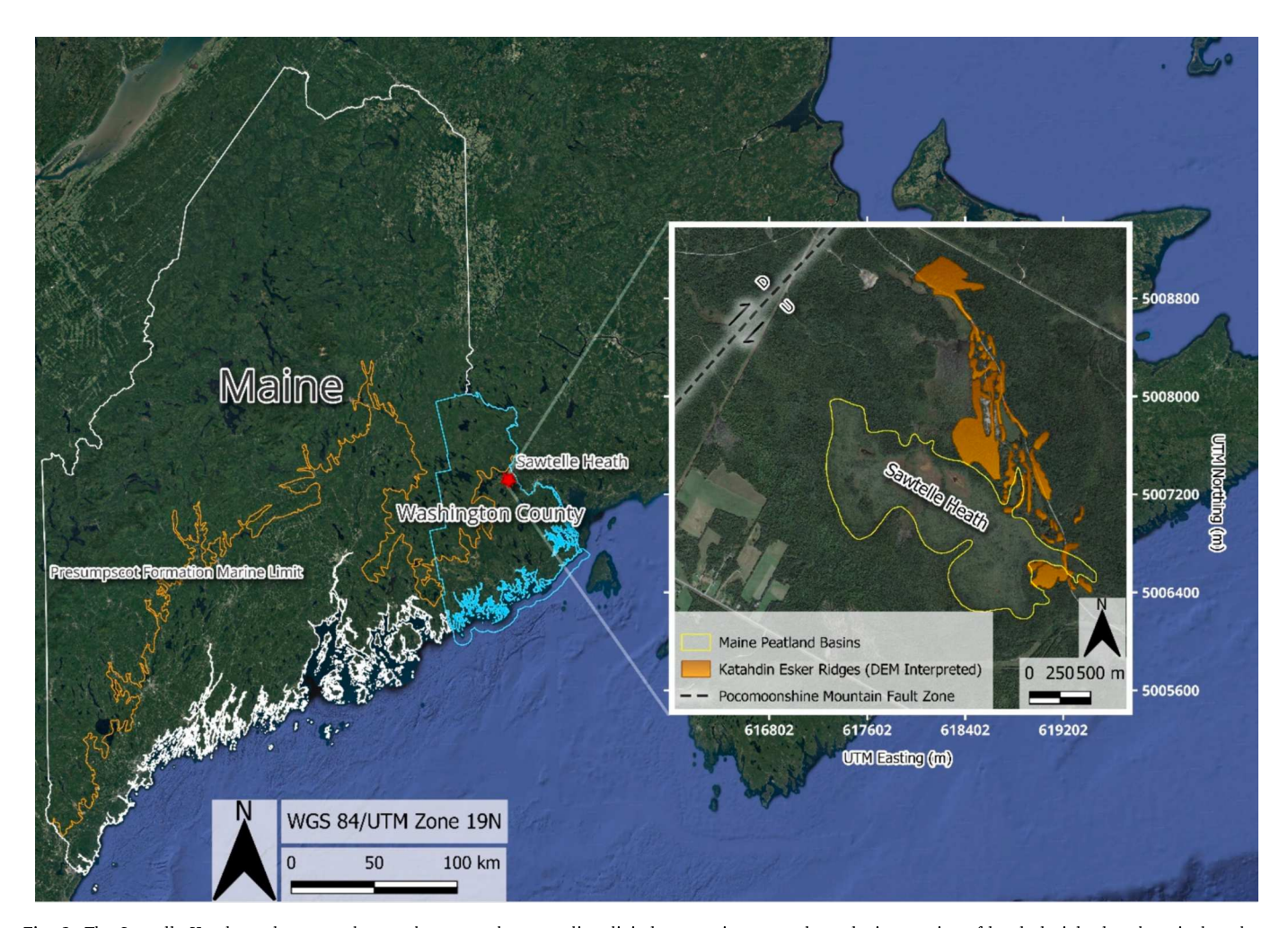


Fig. 2. The Sawtelle Heath northern peat bog study area and surrounding digital reconnaissance-scale geologic mapping of local glacial esker deposits based on elevation. The orange line of the main figure represents the marine limit of the Presumpscot Formation and Washington County is highlighted in light blue. Portions of geospatial data are from the Maine Geological Survey (2016; 2017; 2019). (For interpretation of the references to color in this figure legend, the reader is referred to the web version of this article.)

were disrupted by glacial deposits as the terrain experienced isostatic rebound (Borns et al., 1963). The diminished flow in these basins led to the formation of many northern peatlands of Maine, including the Sawtelle Heath bog (Fig. 2; Hu and Davis, 1995). Multiple studies over the past two decades have revealed discontinuities in the Presumpscot Formation stratigraphy in Maine (Trefethen and Harris, 1940; Borns, 1963; Slater and Reeve, 2002; Comas et al., 2004; Comas et al., 2005; Comas et al., 2011; Chen et al., 2020). These studies suggest that permeable esker deposits in direct contact with the base of northern peat bogs may exert an influence on pool formation. The hydraulic conductivity of the confining glacial deposits has been previously modeled using a value of 8.64 x 10⁻³ m/d (Reeve et al., 2009) based on field measurements made adjacent to a similar peat bog (S.W. Cole, 1992). Hydraulic conductivity of regional esker deposits was calibrated for a model by Reeve et al. (2009) using a value of 8.64 m/d, indicating the ability for these discontinuities to alter hydraulic flows.

The Maine Department of Agriculture, Conservation, and Forestry, (2021) characterizes Sawtelle Heath as a 930-acre bog ecosystem containing three raised dome structures. The Sawtelle Heath basin contains three different pools located in the northeast, southwest, and northwest sections of the basin. In Sawtelle Heath, the northeastern pool is 42 m long (N-S) and has a perimeter of 159 m. Along the southwestern pool, the perimeter was measured to be 352 m, with a length of 98.5 m (N-S). The northwestern pool is 95 m in length (N-S), with a perimeter length of 340 m. Water depths of the pools varied between 2 and 3 m. Pools in the bog are surrounded by bog lawns of Sphagnum moss, Drosera intermedia, Nepenthes, and Utricularia ochroleuca (Maine Department of Agriculture, Conservation, and Forestry, 2021). Focus areas surrounding these pools contain typical dwarf shrubs, including Rhododendron canadense, Chamaedaphne calyculata, Rhododendron groenlandicum, and Kalmia angustifolia growing within Sphagnum (Maine Department of Agriculture, Conservation, and Forestry, 2021). A band of forested peat, consisting of Picea trees, Pinus trees, and high shrubs, separates the northeastern and southwestern pools in Sawtelle Heath (Maine Department of Agriculture, Conservation, and Forestry, 2021). The western section of the northwestern pool is surrounded by tall Picea trees, Pinus trees, and high shrubs (Maine Department of Agriculture, Conservation, and Forestry, 2021).

In this study, heat tracing was used to exploit the distinct temperature contrasts between surficial pool water and mineral sediment groundwater during the summer and winter. Thermal anomalies in the vicinity of the pools were identified using an uncrewed aerial system (UAS) equipped with thermal infrared (TIR) and red-green-blue composite (RGB) cameras, targeted handheld TIR imagery, and point measurements of water temperature (similar to recent studies described by Harvey et al., 2019; Casas-Mulet et al., 2020). Areas with substantial thermal contrasts were targeted for diurnal temperature signal analysis within the upper 11 cm of the peat profile to quantify matrix seepage rates at exchange zones using methods reviewed by Irvine et al. (2017). Contrasts in the specific conductance (SpC) of upwelling groundwater from underlying mineral sediments and peat pore water dominated by recharge of meteoric water were investigated using point SpC measurements in conjunction with the point temperature measurements. Water samples were also analyzed for iron and manganese, trace minerals utilized as diagnostic indicators of groundwater sourced from glacial aquifers rather than meteoric water recharged into the peat matrix (Bendell-Young, 2003; Comas et al., 2004). Variations in the geologic structures along the underlying mineral sediment interface were interpreted as permeable lenses of esker deposits as imaged using ground-penetrating radar (Slater and Reeve, 2002; Comas et al., 2004; Comas et al., 2011).

2.2. Thermal characterization

2.2.1. Uncrewed aerial system (UAS) thermal infrared (TIR) and Red-Green-Blue composite (RGB) mapping

A DJI Mavic 2 Enterprise Advanced (DJI M2EA) UAS (SZ DJI Technology Co., Ltd., Shenzhen, China) was flown to map Sawtelle Heath using TIR and red–green–blue composite (RGB) imagery. The DJI M2EA UAS was dually equipped with integrated TIR and RGB cameras mounted on an integrated gimbal. Sensor resolution of the TIR camera was 640 x 512 pixels with an image frequency of 30 Hertz. A DJI M2EA real time kinematic (RTK) module was mounted to the UAS system prior to flight for increased geospatial accuracy of the UAS imagery. Two separate UAS missions were flown in the afternoon of August 11th, 2022, with light, high cloud cover and an average ambient temperature of 20 °C. Mission flights were mapped and executed using DJI Pilot software on a DJI Smart Controller.

The TIR imagery captured by the DJI M2EA UAS recorded the surface temperature of water in the bog. ThermoConverter software, developed by Aetha Global (2022), was used to convert TIR imagery from the raw radiometric output of the DJI M2EA to radiometric Joint Photographic Experts Group (rJPEG) formats and Tag Image File Formats (TIFFs). The rJPEG files were analyzed using FLIR Tools software to determine the approximate temperature range of investigation (Teledyne, 2018). TIFF files were assigned pixel values (unitless) using the ThermoConverter software to create a cohesive temperature scale (°C) across all images, with a scale of 1 °C equating to a pixel value of 100 (Aetha Global, 2022). This linear scale allowed for immediate reference of the TIR temperature values (°C) captured in each pixel of the 640 x 512 field of view against the pixel values of the overall TIFF image processed in OGIS (QGIS.org, 2022) software. Batch processing was applied to the TIFFs based on the temperature to pixel value ratios to ensure equivalent pixel value scales across all TIR images captured during flights. Agisoft Metashape Professional software was used to create TIR and RGB orthomosaics for the two missions flown in Sawtelle Heath. No ground control points were deployed during the UAS missions, however the TIR and RGB orthomosaic products were georeferenced against satellite imagery using QGIS (QGIS.org, 2022) software.

Harvey et al. (2019) demonstrated the use of linear regression to calibrate apparent temperatures captured in UAS TIR imagery by comparing to direct measured temperature values across several open water baths with varying temperatures. The method also estimates the statistical significance of the temperature bias from the UAS TIR imagery from true temperature values. This directly measured water temperature versus UAS TIR linear regression method was applied in our study. On August 4th, 2022, five metal paint trays (28 x 46 cm) were partially filled with water prior to UAS TIR mapping. Temperatures of the water in each pan ranged from lowest (0 °C) to highest (62 °C) within the range of expected land surface temperatures to be captured by the UAS TIR camera during mission flights. The temperature of the four corners and center (totaling five measurement points) of each filled section of the paint trays was measured using a Digi-Sense Type T Thermocouple Meter (+/- 0.4 °C) (Cole-Parmer, Vernon Hills, IL, USA). The UAS was then immediately hovered three meters above the paint trays and TIR imagery was captured (Supplemental Fig. 1a). Raw TIR imagery of the calibration process was retrieved from the UAS system, and the same five points measured directly in each tray were measured in the UAS TIR imagery by choosing the corresponding pixels. Both direct measurements and UAS TIR imagery temperature measurements were averaged for each pan and regressed. Calibration of TIR maps captured during UAS surveys within Sawtelle Heath yielded a strong linear relationship between pixel temperature measured by the integrated UAS camera and temperature measured by hand (Supplemental Fig. 1b coefficient of determination (R^2) = 0.95). Standard error of the regression was calculated to be 4.07 °C. The temperature scale of the UAS imagery was corrected using the linear equation displayed in Supplemental Fig. 1b.

2.2.2. Point temperature and specific conductance measurements

Point temperatures were measured along the edges of pools at an approximate 10-meter linear spacing using a Taylor MRKT Rapid Response Thermometer (+/- 0.1 °C) (Taylor USA, Oak Brook, IL, USA), attached to a 0.25-meter dowel to avoid diurnal temperature signal effects. The probe was fully inserted into the surface water of the pool and the temperature reading was allowed to stabilize. Point SpC data were collected at a depth of 0.25-meters in pool waters using a ThermoFisher Scientific Orion Star Conductivity Portable Meter (+/- 0.5 % of measurement) (ThermoFisher Scientific Inc., Waltham, MA, USA) with a SpC range of 0.001 μS to 3,000 mS. The conductivity meter was calibrated in the lab prior to fieldwork by using four conductivity standards of 84 μ S/ cm, 1,413 μ S/cm, 12.88 mS/cm, and 111.8 mS/cm. Measurements were acquired approximately every 20 m around the pools and at previously identified temperature anomalies of interest. After each measurement was recorded, the SpC probe was rinsed with deionized water to avoid erroneous cross-sample errors. GPS points were taken with a Garmin GPSMap 64sx handheld unit (+/- 3.65 m) (Garmin International Inc., Olathe, KS, USA) to georeference all point measurements taken. Temperature, SpC, and GPS data were merged, and results plotted over the UAS RGB orthomosaics using QGIS (QGIS.org, 2022) software to examine the spatial distribution of temperature and SpC anomalies

2.2.3. Handheld thermal infrared (TIR) imaging

Handheld TIR imagery was captured in areas of interest (identified using point temperature measurements) to analyze surficial seepage patterns associated with temperature anomalies identified using point measurements in and around pools. Images were acquired using a forward-facing FLIR E8-XT TIR camera (Accuracy: +/- 2.0 °C, Precision: <50 mK) (Teledyne FLIR LLC, Wilsonville, OR, USA) with a sensor resolution of 320 x 240 pixels and image frequency of 9 Hertz. This camera was used for dual RGB and thermal imaging at sites of identified point temperature anomalies. Thermal emissivity of the FLIR E8-XT was set to 0.98, defined as the emissivity of freshwater by Handcock et al. (2012), and the relative humidity parameter was set to a static 50 percent. Shot distance for the thermal imagery ranged between 0.5 m to three meters, depending on the size of the thermal anomaly. Images were taken by targeting the temperature anomaly previously identified, allowing the camera to adjust to the temperature within the field of view, and then capturing the dual imagery. Imagery was collected in late winter of 2022 (expected warmer upwelling groundwater relative to near-surface peat pore water) and in the summer of 2022 (expected cooler upwelling groundwater relative to near-surface peat pore water). The rJPEG imagery was processed using FLIR Tools software to optimize the scale and color used to examine temperature anomalies associated with groundwater seepage processes (Teledyne, 2018).

2.2.4. Vertical temperature profilers and groundwater flux modeling software

Vertical temperature profilers (VTPs) were used to track the propagation of natural temperature signals with depth in the saturated peat soils to quantify peat matrix seepage. Zones of possible groundwater seepage, identified using TIR and point temperature measurements, were selected for VTP installation. Each VTP was built using four temperature loggers installed in a 25-centimeter long, 2.5-centimeter diameter steel pipe filled with foam insulation. Lateral slots were cut into the steel pipe for the installation of the four temperature loggers, similar to the design of Briggs et al. (2014) that was specifically developed to quantify vertical groundwater flow using diurnal temperature signals. Steel piping and foam insulation were used to dampen internal thermal conduction within VTPs that could otherwise lead to erroneous data (Irvine et al., 2017). Four iButton temperature loggers, models DS1922L#F50 (+/- 0.0625 °C) or DS1925L#F50 (+/- 0.0625 °C) (iButtonLink LLC, Whitewater, WI, USA), were programmed and inserted into each VTP prior to deployment. VTPs were inserted into the peat matrix with the iButtons installed at depths of 1, 4, 7, and 11 cm below the surface. The iButton sampling rate was set to one measurement every 30 min in OneWireViewer software (Maxim Integrated, 2009) and data were collected for a continuous 14-day period. Deployments all took place after a period of three days without local precipitation recorded. During the first deployment, a TEMPOS Thermal Properties Analyzer (Meter Group, Inc., Fullman, WA, United States) was used to record the heat capacity, thermal diffusivity, and thermal conductivity. The average values of measured thermal parameters were used in the analytical modeling of groundwater fluxes for the second and third deployments of the VTPs.

Diurnal temperature signal analysis was completed using VFLUX 2 open-source software run in MATLAB, which calculates analytical solutions to the heat transport equation for determining vertical groundwater flux over time between two temperature logger locations (Gordon et al., 2012; Irvine et al., 2015). Dynamic harmonic regression was used to identify and extract non-stationary diurnal signals within the raw data collected when the amplitude of those signals exceeded approximately 1.3 °C (twice the iButton temperature precision). Following suggestions from Briggs et al. (2014) for characterizing groundwater upwelling, the Hatch et al. (2006) solution based on diurnal signal amplitude ratios was selected to calculate analytical solutions for groundwater flux. All flux estimates were calculated using a 0.06-meter window, between the one-centimeter and seven-centimeter loggers, in the VFLUX 2 software based on the median flux values generated over this depth window.

2.3. Water geochemistry analysis

Inductively Coupled Plasma Optical Emission Spectrometry (ICP-OES) was employed to analyze iron and manganese trace elements within water samples. Eleven 250-mL water samples were collected between August and October 2022. Samples were collected at the surface of the pools or stream, transferred to a cooler on ice for travel back to the lab, and kept refrigerated in the lab prior to geochemical analysis. The ICP-OES procedure parallels what was used by Espinoza-Quiñones et al. (2015) to analyze iron and manganese trace elements. A 2 % nitric acid solution was used as the background solution for ICP-OES analysis based on the expected concentrations of trace elements within the samples. A day prior to analysis, six 50-mL standards of iron and manganese ranging from 0 to 5 ppm were prepared as background solutions. Samples were prepared for acidification and filtration by first allowing them to reach room temperature. Samples were shaken by hand to suspend any precipitated solids prior to acidification. Seven mL of each of the eleven samples were acidified using 140 µL of 70 % nitric acid. Samples were then filtered using a 0.22-µm filter to remove remaining suspended organics present after acidification. A 10 % dilution was prepared by separating 0.5 mL of each raw sample and combining this with 4.5 mL of the selected 2 % nitric acid background solution. An Agilent Technologies 5110 ICP OES unit (Agilent Technologies Inc., Santa Clara, CA, USA) paired with an Agilent Technologies SPS 4 Autosampler was used to analyze the samples with six standards. The autosampler was rinsed using 5 % nitric acid solution after each sample was tested. Calibration of the spectral peaks throughout the geochemical analysis was done using three quality check solutions prepared with the three-ppm standards that were intermittently sampled by the ICP-OES unit.

2.4. Ground-Penetrating radar surveys

Ground-penetrating radar (GPR) was deployed to image peat stratigraphy and capture the architecture of the peat-mineral soil interface, which yielded insights into proposed hydrogeologic controls on the surface hydrology. The GPR unit transmits an electromagnetic (EM) wave into the near surface that travels back to a receiver which records reflections from interfaces exhibiting contrasts in relative dielectric permittivity ($\epsilon_{\rm r}$), which is primarily determined by water content,

particularly in peat soils (i.e., Theimer et al., 1994). The velocity of the EM wave from the GPR antenna is governed by ε_r . The transmissivity of the EM wave below the peat stratigraphy provides spatial information on discontinuities in the mineral sediment based on the amplitude of the reflection along the peat-mineral sediment interface. Both 50 MHz and 100 MHz MALÅ rough terrain antennas (RTAs) (MALÅ Geoscience AB, Malå, Sweden), paired with a MALÅ ProEx acquisition system, were used for GPR data collection. RTAs were dragged behind a snowmobile during data collection in the late winter of 2022. GPS coordinates were continuously recorded by a Trimble GPS unit (Trimble Inc., Westminster, CO, USA) during data collection. GPR datasets were processed using GPRPy software (Plattner, 2020). GPR data processing was limited to applying a zero-time correction, using a 'dewow' filter to remove low frequency DC bias, and applying a time-power gain correction to amplify the signal with depth. An average EM wave velocity value of 0.036 m/ ns, typical of peat soils in Maine, was used to determine profile depths (Comas et al., 2005). This was determined to be a reasonable assumption when looking for spatially large glacial structures at the basin scale, despite likely variable gas accumulation at finer scales throughout the basin (Comas et al., 2007).

3. RESULTS

3.1. Thermal characterization

3.1.1. Uncrewed aerial system thermal infrared mapping

Analysis of the TIR orthomosaic maps generated from the August 2022 UAS surveys revealed numerous, localized thermal anomalies indicative of cool upwelling groundwater into and adjacent to pools. The TIR map over the central section of Sawtelle Heath (Fig. 3 (a-d)) yielded an average pool surface temperature of 26.7 °C for the northeastern pool and 27.9 °C for the southwestern pool, excluding discrete cooler anomalies. The average surface temperature of the northwest pool, excluding the cool thermal anomalies, was 25.2 °C in the TIR map. Fig. 3a contained a surficial temperature of 16.7 °C, with a thermal gradient originating from the southeastern corner of the southwestern pool. The observed surface water temperature gradient showed the northward seepage of cooler water away from this location. A similar pattern was observed in Fig. 3b, where cooler water from the southeast corner of the northeastern pool displayed a temperature gradient that displayed northward seepage. Additionally, point temperatures of 18.9 °C and 19.3 °C are observed in the UAS TIR imagery (Fig. 3c). The band of forested peat separating the northeastern and southwestern pools highlighted a strong temperature contrast in the landscape identified as a line, associated with a stream flowing northwest/north, that originated at the southernmost end of this vegetation (Fig. 3d). This stream was found to have a depth of 0.5 m in the deepest section. Reconnaissance-scale field mapping from satellite imagery did not identify this stream prior to the deployment of the UAS TIR mapping. The preferential discharge point that appeared to primarily source this stream was characterized by a low temperature of 12.9 °C, the coolest surficial temperature observed in the TIR orthomosaic maps. Fig. 3e showed thermal evidence of seepage into the southwestern corner of the northwestern pool, with a cooler temperature of 21.9 °C.

3.1.2. Point temperature and specific conductance measurements

Point temperature measurement patterns are generally spatially consistent with the TIR orthomosaic maps generated from the drone imagery (Fig. 3 and Fig. 4). Points of low temperature corresponded with high SpC point anomalies in the pools between the two datasets. High SpC values were recorded surrounding the northwestern pool with measurements ranging from 99.1 μ S/cm to 120.2 μ S/cm. Lower SpC and higher temperature values were observed along the eastern side of this pool (Fig. 4b). Similar point temperature and SpC patterns were observed in the southwestern pool (Fig. 4a). A low temperature of 9.9 °C and a relatively high SpC of 102.8 μ S/cm were recorded in the

southwestern corner of this pool. Temperature increased and SpC decreased moving northward around the pool. Cold water was measured along the stream separating the northeastern and southwestern pools, with the lowest temperature of 7.4 °C recorded in this dataset found at the headwaters of the stream (Fig. 4a). This location yielded a low SpC of $60.2 \,\mu\text{S/cm}$. Consistent with the TIR map, the temperature of the stream was on average cooler than the pools, ranging between 12.5 °C and 18.9 °C. Low temperature anomalies occur within the vicinity of locations NE2 and NE3, with a minimum temperature of 15.7 °C (Fig. 4a). Elevated SpC values, with a maximum of 184.5 µS/cm, were recorded at these locations. A low temperature anomaly of 17.7 °C was also recorded in the southwestern corner of this pool, with an associated relatively high SpC of 94 µS/cm. Temperatures increase moving northward in this pool, before decreasing as the pool meets the stream. SpC decreased steadily moving northwards around the pool. Linear regressions plotting point temperature versus SpC were analyzed to determine the relationship between the two datasets (Supplemental Fig. 3). The coefficients of correlation (R²) of the regressions were used to show the linear relationships between the two point measurements in the pools and p-values (p) were analyzed for statistically significant relationships between the variables (p < 0.05). The northeastern pool was found to have the lowest R^2 of 0.49, with p = 0.0050 (Supplemental Fig. 3a). Data collected around the southwestern pool yielded an $R^2 = 0.65$ and p =0.0016 (Supplemental Fig. 3b). Data from the northwestern pool yielded statistical values of $R^2 = 0.65$ and p = 0.0009 (Supplemental Fig. 3c). Anomalies highlighted in the TIR orthomosaics, point temperature measurements, and point SpC measurements were used to select for further seep-scale analysis (Fig. 4, Supplemental Table 1).

3.1.3. Handheld thermal infrared imaging

Handheld TIR image stills collected during cold and warm seasonal conditions highlighted fine-scale patterns of seepage originating from localized upwelling of groundwater. Distinct seepage patterns were observed around both PFP and porous media sources during both the summer and winter seasons. For example, two handheld TIR images (Fig. 5) provided fine-scale spatial mapping of two selected thermal anomalies also identified in UAS TIR orthomosaics (Fig. 3). Handheld TIR imagery showed relatively cool groundwater at sampling location STR1 in the summer (Fig. 5a) and relatively warm groundwater at sampling location SW3 in the winter (Fig. 5b). Evidence for three distinct points of cooler temperature was found at sampling location STR1 (Fig. 5a). The heterogenous nature of the thermal signal of the seepage observed in Sawtelle Heath is highlighted at sampling location SW3 (Fig. 5b). Supplemental Fig. 4 shows similar heterogeneous seepage patterns observed using handheld TIR imaging at sampling locations NE2, NE3, and NE4 in Sawtelle Heath.

3.1.4. Vertical temperature profilers

Multi-depth temperature time series were recorded using VTPs at six of the targeted point sampling locations during summer 2022 (Fig. 6). Daily precipitation data captured at the NOAA (2022a; 2022b; 2022c) weather station, located 22 km away in Grand Lake Stream, Maine, were included in the analysis to examine meteorological influences on vertical flux at VTP locations. Measured diurnal temperature signals include periods of high attenuation of signal amplitude along with clear thermal gradients (towards cooler water) with depth (e.g., Briggs et al., 2014). During discrete time periods the multi-depth temperature time series converge and track at similar, cooler values. Processing these "convergent" portions of the datasets in VFLUX 2 was not possible due to the underlying assumptions of the method discussed previously (i.e., a general lack of identifiable diurnal signals, indicating potential PFP flow). Vertical water flux through the peat matrix was modeled using VFLUX 2 for the first deployment of the VTPs from August 12th, 2022, to August 18th, 2022, at targeted points STR1 and SW3 (Fig. 6a and 6b). Convergent data at both points were observed from August 18th, 2022, until the end of the deployment. The second deployment of the VTPs at

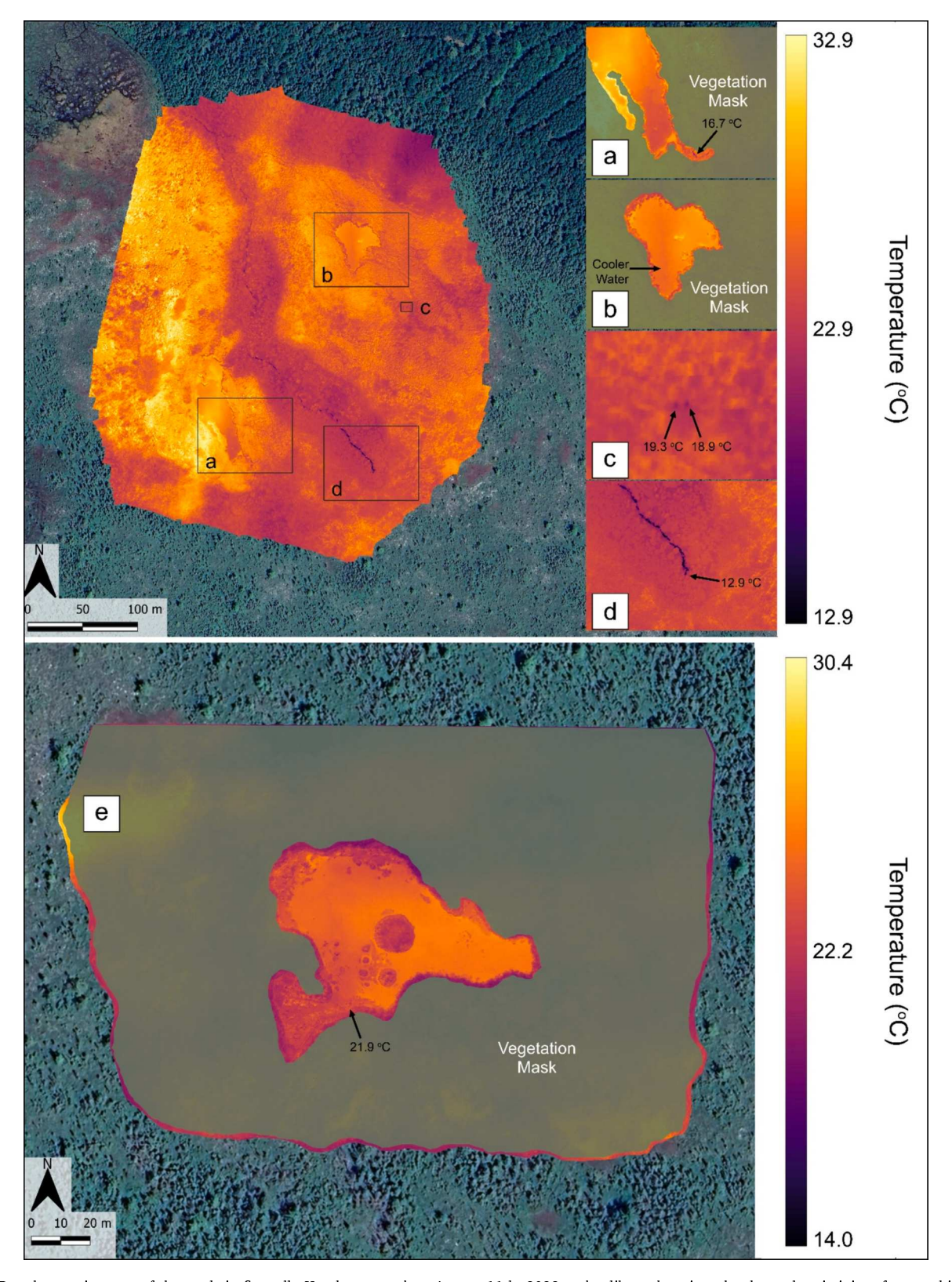


Fig. 3. TIR orthomosaic maps of the pools in Sawtelle Heath captured on August 11th, 2022 and calibrated against the thermal emissivity of water, highlighting features including: (a) surficial mixing dynamics in the southwestern pool, originating from a cool temperature anomaly in the southern portion of the pool, (b) cool temperature anomalies around the northeastern pool expressing seepage northwards, (c) cool point temperature anomalies expressed at the surface, (d) temperature anomalies originating from the headwaters of a stream separating the northeastern and southwestern pools, and (e) a cooler temperature anomaly in the northwestern pool, indicative of seepage originating from the southwestern corner. Vegetation masks are applied to (a), (b), and (d) to highlight pool temperatures. Resolution for (a)-(d) is 8.06 cm/pixel and 11.2 cm/pixel for (e). Corresponding RGB imagery is available in Supplemental Fig. 2 for (a)-(e).

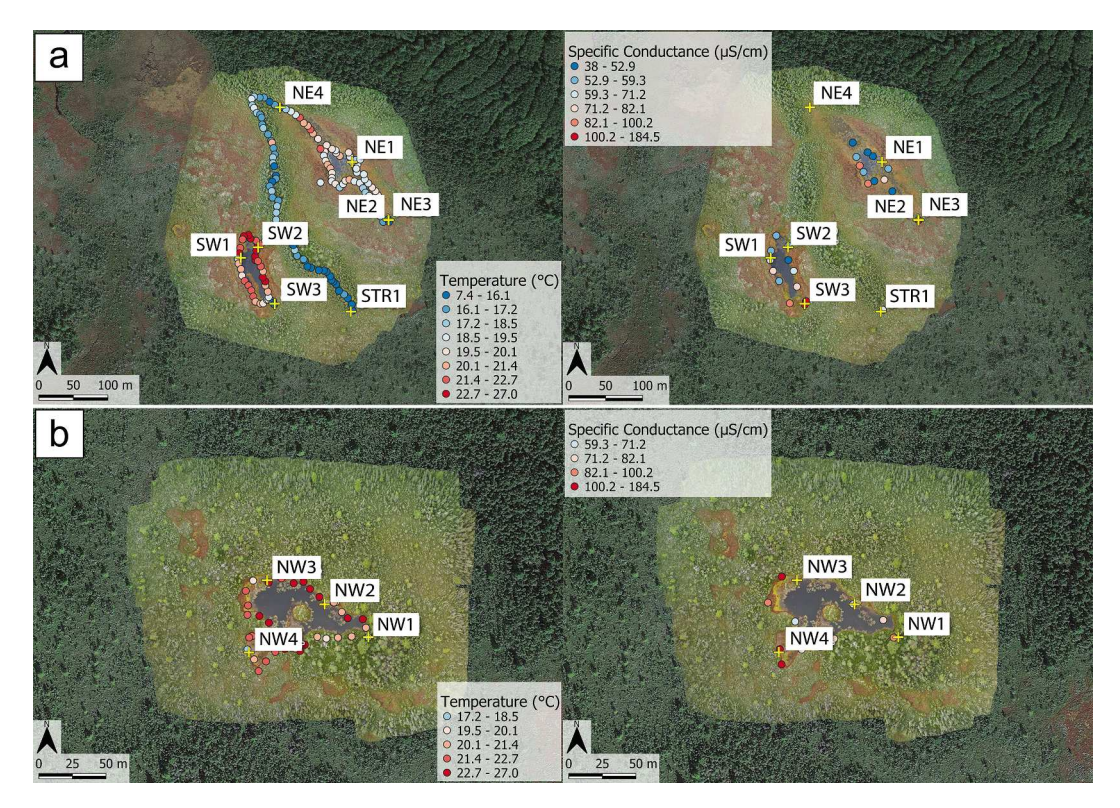


Fig. 4. Point temperature measurements taken at 0.25 m depth, collected over the course of August 11th to 12th, 2022, and point SpC measurements taken at 0.25 m depth, collected on October 5th, 2022, around the (a) stream (STR1), northeastern pool (NE1-NE4), and southwestern pool (SW1-SW3), (b) northwestern pool (NW1-NW4). Targeted point sampling locations are highlighted by yellow crosses and labeled according to hydrologic features. Point measurements are overlaid on the red–green–blue composite (RGB) orthomosaics produced from UAS imagery. (For interpretation of the references to color in this figure legend, the reader is referred to the web version of this article.)

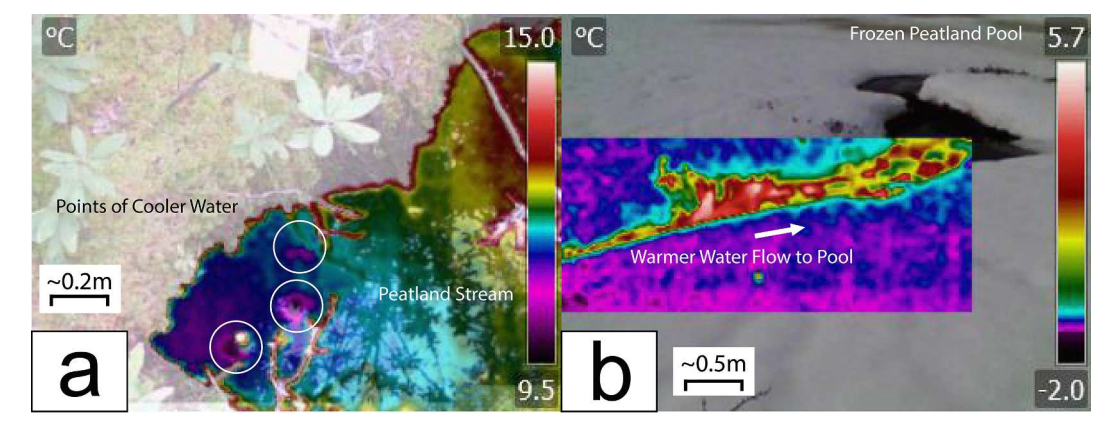


Fig. 5. Example handheld TIR image overlaid on the RGB image of (a) point sources (highlighted by white circles) of cool water at the headwaters of the stream (STR1), taken at 11:35 on August 17th, 2022, during the summer season, and (b) seepage of warm water feeding the southwestern pool (SW3), taken at 15:58 on February 10th, 2022, during the winter season.

targeted points NE4 and NE2 yielded vertical flux that could be modeled from September 10th, 2022, to September 20th, 2022 (Fig. 6c and 6d). Raw temperature with depth values at these points converged on September 20th, 2022, and remained convergent until the end of the deployment. Targeted points NE3 and NW4 during the third deployment of the VTPs had the greatest variation in vertical flux values that could be modeled. Vertical flux estimates were modeled from October 9th, 2022, to October 14th, 2022, for targeted point NE3, where convergent data were observed from October 14th, 2022, until the end of the deployment (Fig. 6e). In contrast, vertical flux estimates were modeled from October 5th, 2022, until the end of the third deployment at location NW4 (Fig. 6f).

Time periods of VTP data convergence appear to correspond with notable precipitation events (Fig. 6). During the period of August 11th, 2022, to August 27th, 2022, the first deployment of the VTPs showed strong convergence at similar temperatures across the profile, and absence of diurnal signals beginning on August 18th, 2022 (Fig. 6a and 6b). This corresponded to the most notable precipitation event in the month of August, with 28.1 mm of rain beginning on August 18th, 2022. During the second deployment of the VTPs from September 9th, 2022, to September 23rd, 2022, a similar signal convergence occurred at NE4 and NE2 starting on September 20th, 2022 (Fig. 6c and Fig. 6d). This event paralleled the multi-day precipitation event, observed from September 19th, 2022, to September 23rd, 2022, when 112 mm of

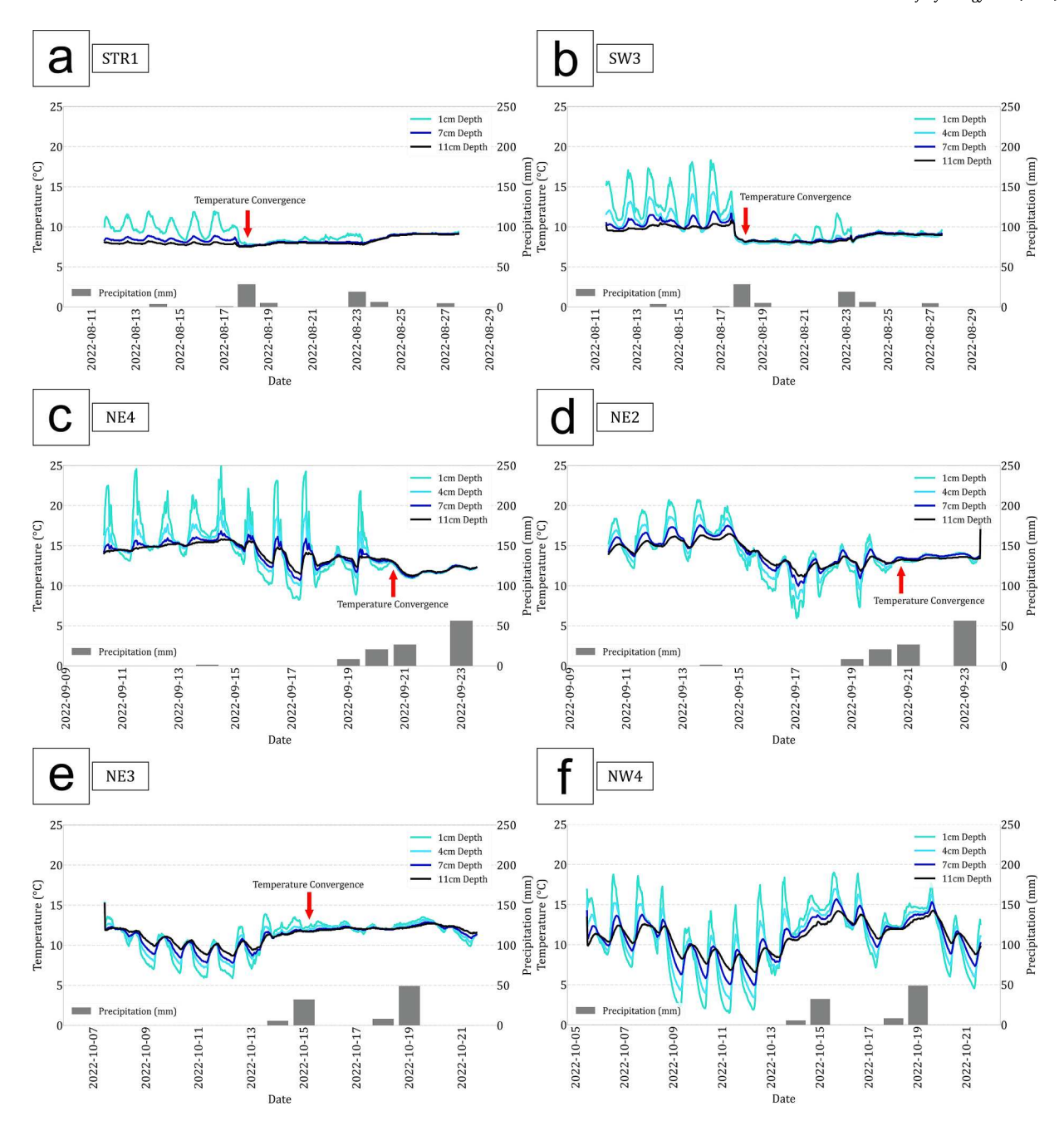


Fig. 6. Raw temperature data with depth from the vertical temperature profilers (VTPs) installed between August 2022 to October 2022 at (a) STR1: the headwaters of the stream (only three depths of the temperature loggers were used due to the failure of the four centimeter depth iButton), (b) SW3: the input to the southwest pool, (c) NE4: the confluence of the northeastern pool and stream, (d) NE2: a southeastern input to the northeastern pool, (e) NE3: a southeastern input to the northeastern pool, and (f) NW4: the input to northwestern peatland pool. Daily (data recorded every 24 h) precipitation data (NOAA, 2022a; NOAA, 2022b; NOAA, 2022c) are plotted for comparison.

precipitation was recorded. The raw diurnal temperature signals from the third VTP deployment from October 5th, 2022, to October 21st, 2022, only measured approximately constant temperature at NE3. The near-constant temperature measured at NE3 corresponded to notable precipitation recorded from October 14th, 2022, to October 19th, 2022, totaling 95 mm. However, upwelling signals within the raw data at NW4 corresponded well with the same notable precipitation event (95 mm) recorded between October 14th, 2022, and October 19th, 2022.

Flux estimates generated using VFLUX show consistent matrix upwelling during the VTP deployments in August and September in Fig. 7. Vertical upwelling is presented as positive flux (m/d) and vertical downwelling is presented as negative flux (m/d) for these datasets (Fig. 7). The strongest, most consistent upwelling, highlighted in Fig. 7a,

was found at the source of the stream (STR1) and at the input to the southwestern pool (SW3) during the first deployment of the VTPs. The average vertical specific discharge (flux) at STR1 was 0.190 m/day (m/d), with a maximum of 0.239 m/d. Location SW3 displayed an average vertical flux of 0.339 m/d and a maximum vertical flux of 0.391 m/d during the August VTP deployment. Flux estimates declined over time at both locations up until August 18th, 2022, representing the beginning of the period when diurnal temperature signals converged. Flux estimates at NE4 are shown in Fig. 7b, which exhibited a decline in upwelling until September 15th, 2022, when signals flatlined. A rebound to upwelling signals at this location is observed on September 19th, 2022, prior to the convergence of diurnal temperature signals. The average vertical flux at NE4 was 0.150 m/d over the deployment, with a

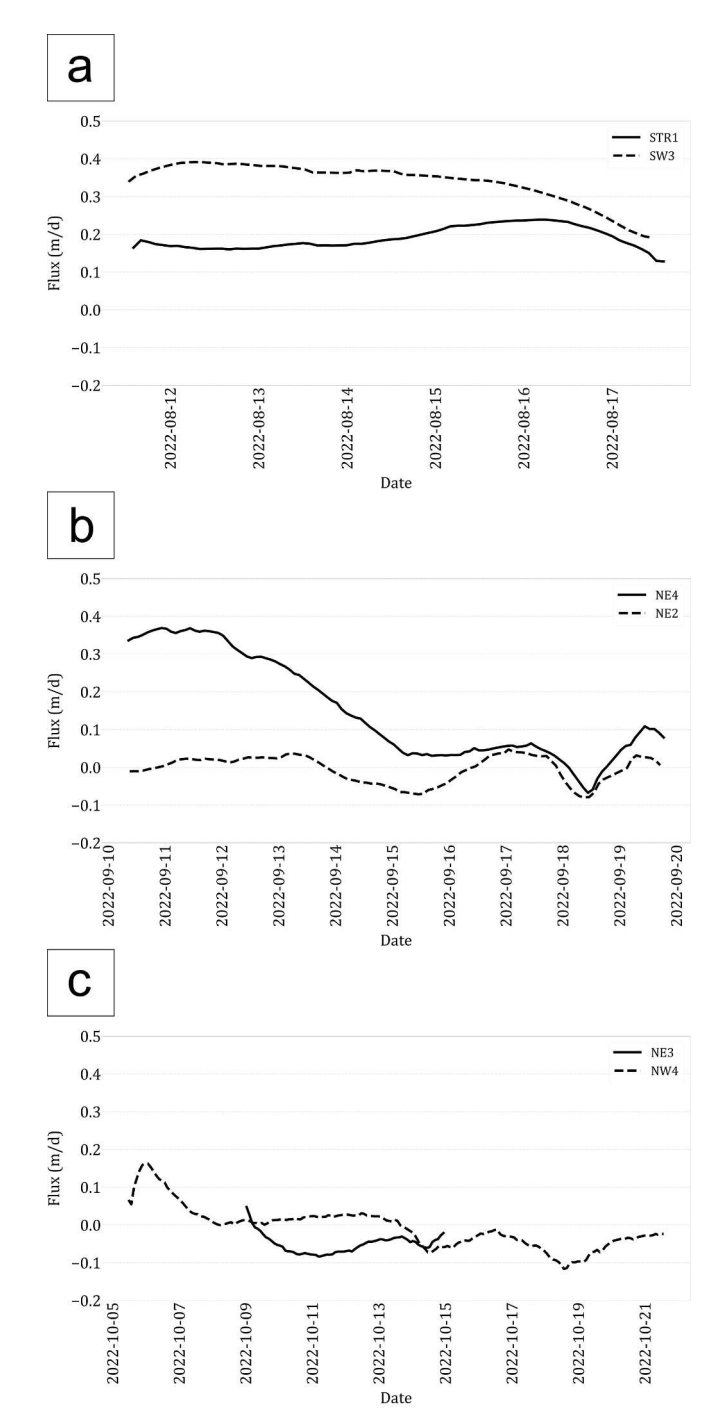


Fig. 7. Vertical discharge fluxes (+/- 0.1 m/d), where positive flux indicates upwelling water, modeled at 0.06 m depth using VFLUX 2 during; (a) the August VTP deployment at STR1 and SW3, (b) the September VTP deployment at NE4 and NE2, (c) the October VTP deployment at NE3 and NW4.

maximum vertical flux of 0.369 m/d. Location NE2 showed negligible flux, averaging -0.005 m/d, with a maximum vertical flux of 0.047 m/d, before the convergence of the diurnal temperature signals on September 20th, 2022 (Fig. 7b). A summary of flux estimates for NE3 and NW4 are shown in Fig. 7c. NE3 began with slight upwelling before minimal flux was observed, with an average vertical flux of -0.050 m/d and a maximum vertical flux of 0.047 m/d. Flux estimates at NW4 showed similar evidence of initial upwelling prior to a period of minimal flux to the pool with an average vertical flux of -0.006 m/d and a maximum vertical flux of 0.162 m/d. All vertical discharge fluxes were assumed to have a precision of +/-0.1 m per day based on the findings of

Briggs et al. (2012) when deploying this method. All downwelling modeled using VFLUX fell within the precision error defined by Briggs et al. (2012) and was therefore unable to be confirmed as such with confidence.

3.3. Water geochemistry analysis

ICP-OES analysis yielded systematic variations in iron and manganese trace element concentrations within the eleven surficial water samples acquired from targeted point sampling locations. Iron and manganese trace elements were expected to originate from anaerobic processes associated with mineral grains in the local, shallow glacial aquifer (Baker et al., 2000). Analytes of iron (wavelength = 234.35 nm) and manganese (wavelength = 257.61 nm) were selected as the best fit wavelengths based on the instrument regression calibration during geochemical analysis. Low concentrations of iron and manganese were observed in samples collected at points NW2, NW3, and NW4 around the northwestern pool (Fig. 8). The water sample collected at NW1 is an outlier around the northwestern pool, showing an intermediate concentration (Fig. 8). Sampling point SW3 displayed a high concentration of these trace elements, while intermediate concentrations in samples collected at points SW1 and SW2 are nearly halved. The water sample collected at STR1 displayed the highest concentrations of manganese sampled. Water samples collected at points NE1, NE2, and NE3 also showed high concentrations of iron and manganese. The raw and diluted geochemical samples yielded similar concentration results, giving confidence in the ICP-OES analysis procedure.

3.4. Ground-Penetrating radar surveys

GPR surveys resolved the peat stratigraphy and identified the depth of the mineral sediment interface across Sawtelle Heath. Surveys revealed a lack of reflections beyond three to five meters depth over most of the study area. Transect F (Fig. 9) shows an example of the observed lack of reflections between 400 m and 470 m. A lack of reflections beyond this point with depth implies the complete attenuation of the EM wave emitted from the instrument. This transect further highlights one of many discontinuities observed intermittently along the mineral sediment interface, displayed by a ridge geometry from 470 m to 540 m. The crest of the ridge is observed at 531 m within Transect F. Transect C (Fig. 9) displays another ridge structure with a crest at 361 m. Crests of these discontinuities continue to the southwest, represented by the blue triangles shown on Transects C and F (Fig. 9). The path taken during data acquisition limited identification of the crests of the underlying ridges but provided valuable insight into the locations of these deposits. Transect A shows an example of data collected along a meandering path showing the underlying ridge deposit without a visible crest. Variations in the mineral sediment corresponded well with the observed locations of upwelling highlighted in Fig. 7 and Fig. 8. Additional GPR profiles highlighting discontinuities along the peat-mineral sediment interface are available in the Supplemental Materials (Supplemental Fig. 6).

4. DISCUSSION

The hydrogeophysical datasets collected for this study suggest evidence of preferential groundwater discharge sourced from permeable esker sediment deposits and directly feeding peatland pools. Basin-scale orthomosaics generated from UAS TIR imagery illuminate lateral seepage patterns in pools and highlight preferential inputs across the peatland (Fig. 3). Preferential seepage of water from depth is further confirmed using handheld TIR imagery and point scale temperature measurements (Fig. 5). These methods allude to seepage feeding pools via PFPs associated with peat pipes (e.g., void/conduit flow) and through the peat matrix (e.g., Darcian porous media flow). Additional thermal characterization during the winter season further supports the

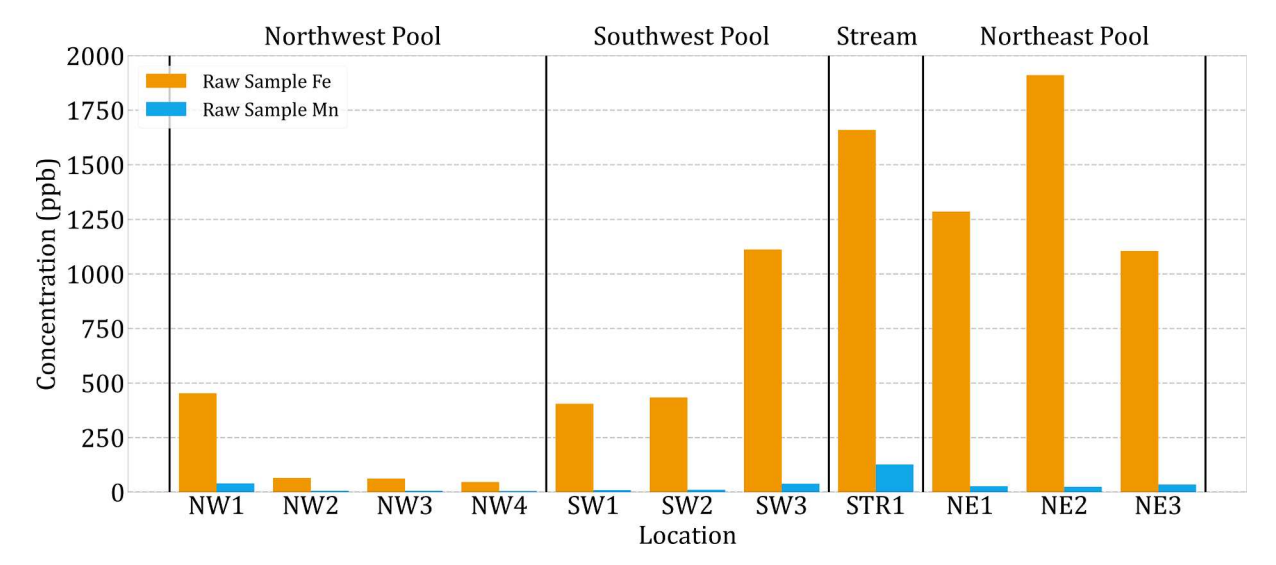


Fig. 8. Iron (Fe) and manganese (Mn) concentrations in the water samples collected at 11 targeted sampling locations. Concentrations were determined using inductively coupled plasma optical emission spectrometry (ICP-OES).

upwelling of water from depth, with warmer water observed at the surface of these seepage locations that would not be expected without direct groundwater to surface connectivity. Peat matrix seepage rates into pools, quantified using VTPs, show high rates of vertical upwelling in multiple locations of deployment, with times of VTP signal convergence qualitatively indicating the activation of peat piping adjacent to measurement locations (Fig. 6 and Fig. 7).

Water transport from the local permeable aquifer to the surface appears to be partly facilitated by peat piping within the organic matrix. Highly localized thermal anomalies were observed in the UAS TIR imagery surrounding the pools (Fig. 3c), some interpreted as surficial terminations of pipe features delivering cool water from depth in the summer (Fig. 4; Supplemental Fig. 5; Supplemental Video 1; Supplemental Fig. 7). Although direct evidence for peat pipe connectivity to underlying mineral sediment is not presented in this study, observations of such surficial peat pipe terminations support this transport model. These terminations were characterized by round voids (Supplemental Fig. 5; Supplemental Fig. 7) indicative of underlying high hydraulic conductivity channels, similar to the observations made by Holden and Burt (2002) and Hare et al. (2017). Surficial terminations of suspected pipe structures were visually noted at the surface when traversing around pools (Supplemental Fig. 7). Unique vegetation patterns were also observed around the terminations of peat pipes throughout the peatland. The most striking of these was found surrounding the peat piping terminations south of the northeastern pool, shown in Supplemental Fig. 5. These vegetation communities suggest the discharge of minerogenous groundwater to isolated portions of the peat surface (Supplemental Fig. 5; Le Maitre et al., 1999). Peat pipes have been well documented to transport water laterally in natural peatlands (Holden and Burt, 2002; Baird et al., 2009) and water from depth vertically in an anthropogenically modified cranberry peatland (Hare et al., 2017). Rossi et al. (2012) report evidence suggesting that vertical peat pipe conduits can extend to depths of 8.0 m when overlying a glaciofluvial (esker) aquifer, encouraging the interpretation of pipe structures observed in Sawtelle Heath extending with depth. However, pipes have never previously been interpreted to link the upward vertical flow of water from depth to supply natural pools or other focused discharge points in a peat bog.

Previous hydrological models show flow cells within the peat matrix promote vertical upwelling of peat pore water from depth (Reeve et al., 2000; Reeve et al., 2009). Therefore, the source of upwelling water discharged at these seeps could theoretically be meteoric water contained in the deep peat. However, the geochemical data indicate that

groundwater originating in glacial sediments is sourcing the preferential seepage into the peatland pools. Elevated SpC around upwelling zones suggest the input of groundwater sourced from glacial deposits below the peatland. Statistically significant linear relationships between temperature and SpC data enhance the argument for minerogenous groundwater reaching the surface of pools within the bog. Geochemical analysis of surface water samples from eleven points of interest revealed high concentrations of iron and manganese relative to the expected negligible amounts found in meteoric water. Iron and manganese are common trace elements found in groundwater originating from glacial aquifers, being consistent with the local glacial esker deposits observed at the eastern edge of the peatland (Bendell-Young, 2003). Further, concentrations of iron and manganese determined in this study are consistent with the range (Fe: 3.00 ppb -38,100 ppb, Mn: 0.056 ppb -28,200 ppb) identified by Groschen et al. (2009) for groundwater originating from glacial aquifers in the northern United States.

GPR datasets indicate that underlying permeable deposits come in contact with the base of the peatland. Peat thickness in Sawtelle Heath was interpreted to range from a minimum depth of 0.31 m to a maximum depth of 5.7 m. Attenuation of the EM wave beyond a certain depth in GPR surveys was indicative of the Presumpscot Formation, an electrically conductive glacio-marine clay that acts as a hydraulically confining layer in many northern peatlands of Maine (Slater and Reeve, 2002; Comas et al., 2004). Transitions from the highly conductive clay to a coarse-grained discontinuity show the increased penetration from the EM wave (Fig. 9, Transect F). The increased transmissivity of the EM wave beneath the peat was attributed to the presence of coarse-grained (presumably high permeability) esker deposits in contact with the peat. GPR transects identify well-defined esker ridges linearly crossing westward beneath the pools from the upland glacial esker deposits of Fig. 1. These ridges resemble the glacial esker systems imaged beneath Caribou Bog, a well-studied peatland about 103 km south of Sawtelle Heath (Comas et al., 2004; Comas et al., 2005, Comas et al., 2011, Chen et al., 2020). Findings further parallel those of Hare et al. (2017) in which seepage through a peat matrix was also investigated using heat tracing and GPR methods. However, there are distinct structural geologic differences driving groundwater upwelling to the northern pools. Permeable glacial deposits surround and underly the anthropogenically modified cranberry bog investigated by Hare et al. (2017), while the natural bog of Sawtelle Heath is largely hydraulically bound by impermeable clays along the peat-mineral soil interface. Distinct ridges, imaged using GPR, highlight the discontinuities in this clay and spatially correspond to zones of groundwater upwelling. Portions of the GPR data

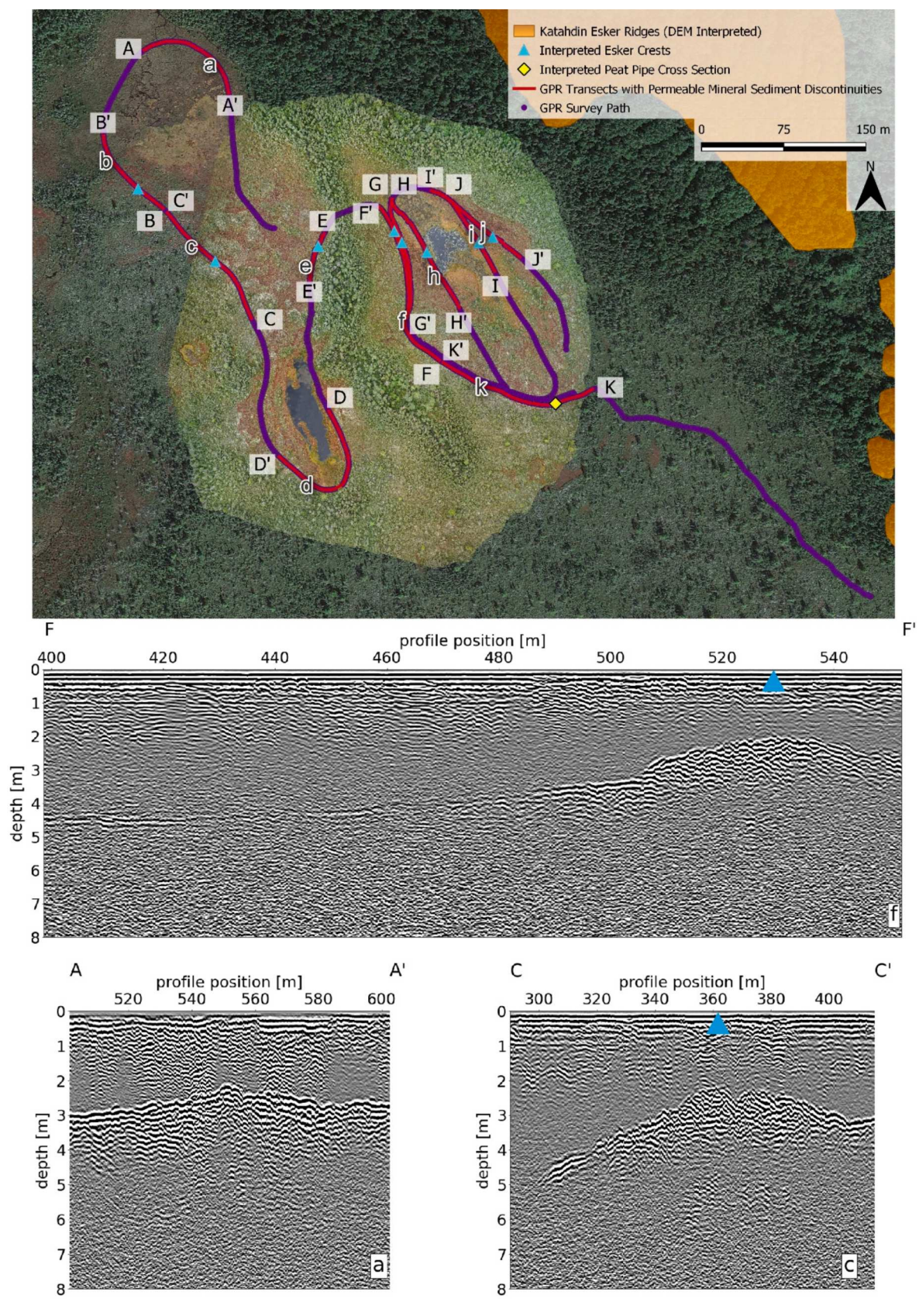


Fig. 9. Selected ground-penetrating radar (GPR) profiles with subsurface coarse-grained discontinuities and their crests (blue triangles) along the peat-mineral sediment interface, collected in February 2022. (For interpretation of the references to color in this figure legend, the reader is referred to the web version of this article.)

show that these ridges could be in direct contact with the pools, leading to direct exchanges of water independent of the hypothesized peat pipe conduits. This spatial evidence implies underlying glacial esker deposits in direct contact with the peat matrix and pools could serve as the origin of groundwater feeding the pools.

Unlike the pools, elevated SpC values were not measured at the stream seepage zone (STR1). This suggests a different source of the upwelling flux into this stream. Despite the low SpC value, geochemical analysis of the STR1 water sample from the headwaters of the stream did show high iron concentrations and the highest observed manganese concentrations observed in this peatland. Based on these differences in aqueous geochemistry and temperature relative to the pool water sources, upwelling water could originate from a deeper bedrock aquifer. Mapped complex bedrock structural geology suggests that fracture induced flow from the underlying Flume Ridge Formation is plausible (Ludman, 1990; Ludman and Hill, 1990). The low-grade metamorphic nature of the siltstone to slate comprising the underlying Flume Ridge Formation may explain the high values of iron and manganese trace elements at the surface if fracture flow sources upwelling into the stream (Penrose, 1893). Fracture induced flow from underlying bedrock could lead to the unique, linear stream hydromorphology observed in Sawtelle Heath. We recognize that differences in geochemistry could also indicate biases within the analysis, with potential inputs from atmospheric iron and manganese leading to sample contamination.

An upward hydraulic head gradient is required to transport groundwater from the underlying glaciofluvial aquifer into the peatland and to the surface of the pools. Previous studies in minerogenous fens have indicated that connections to mineral deposits driving groundwater fluxes show a strong dependence on precipitation (Rossi et al., 2012; Ferlatte et al., 2015; Bourgault et al., 2019). Fens indicate lateral inputs (Ferlatte et al., 2015; Bourgault et al., 2019) and vertical inputs (Rossi et al., 2012) of minerogenous waters driven by local recharge from precipitation. Data from Sawtelle Heath suggest the upward hydraulic head gradient is driven in part by the recharge of contiguous permeable eskers adjacent to the peatland. The influence of local precipitation recharging the local aquifer and driving vertical groundwater inputs to ombrotrophic raised bogs has never been recognized before. Prior studies in minerogenous fens further emphasize the localized nature of groundwater inputs (Rossi et al., 2012; Hare et al., 2017), with higher discharge rates occurring after significant precipitation events. This correlates with the timing of diurnal temperature signal convergence events within the VTP data. Data are interpreted to highlight the rapid response of peat pipe activation and seepage shortly following notable local precipitation, rather than more regional groundwater connectivity. Fig. 6 (a-e), shows the diurnal signal consistently converging across depths, muting the daily signals. This behavior has been interpreted to be indicative of extremely high upwelling rates and/ or preferential flow through macropores where there is little conductive heat transfer from the land surface downwards and the VTPs are dominated by upward groundwater heat advection (e.g., Briggs et al., 2016; Hare et al., 2017). Our data therefore suggest that local precipitation pressurizes the underlying glaciofluvial aquifer via recharge (Waswa and Lorentz, 2019) and drives high vertical upwelling rates to the peat bog pools.

Based on our findings, we present several conceptual hydrogeologic models over time that incorporate upwelling, sub-peat groundwater feeding pools via preferential flow networks. Past peatland hydrological models mainly focus on peat pore water flow at the basin scale, with vertical fluxes being primarily associated with flow cells developing in peat pore water (Reeve et al., 2001; Reeve et al., 2006). Basin-scale groundwater flow has been incorporated into previous models in a variety of peatland hydrogeologic settings (Siegel and Glaser, 1987; Glaser et al., 1997), but sub-peat groundwater has not been specifically modeled to contribute to surface water bodies such as pools. More recent hydrologic models go further to emphasize the role of contrasts in the permeability of the underlying mineral sediment for the development of

these flow cells (Reeve et al., 2009). However, vertical upwelling to peatland pools has only been attributed to cycling peatland (meteoric recharge) pore water, rather than groundwater sources from permeable soils (Reeve et al., 2009). Downwelling of pore water beneath peatland pools has also been previously modeled in publications, indicating that vertical flowpaths may change direction with time (Reeve et al., 2009; Bon et al., 2014).

Data collected in Sawtelle Heath indicate that groundwater recharge from the local underlying glaciofluvial aquifer is the primary driver of vertical seepage to pools. Our conceptual models incorporate hydrologic changes with the peat in response to variations in recharge of the glaciofluvial aquifer. During periods of minimal recharge of the local glaciofluvial aquifer, such that head differences between the esker deposits and peatland pools are minimized (Fig. 10a), vertical upwelling to pools would be primarily dominated by internal peat matrix flow cells

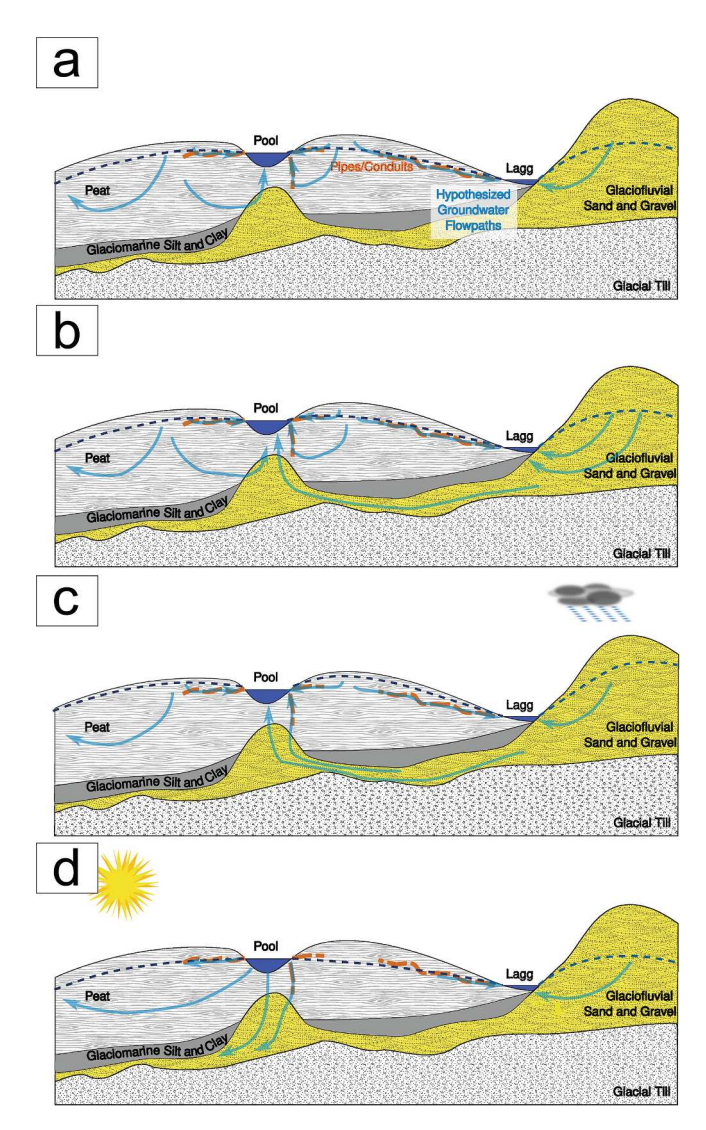


Fig. 10. (a) conceptual model of peatland hydrogeology incorporating vertical upwelling driven by peat pore water flow over changes in the topography and permeability of the underlying mineral sediment (modified from Reeve et al., 2009). (b) Groundwater upwelling originating from permeable glacial deposits, plumbed through both lateral and vertical peat pipes/conduits, mixes with peat pore water, and discharges at the surface. (c) Conceptual model of the hydrogeology of northern peatlands during periods of intense local precipitation (25 mm/d or greater), with enhanced groundwater discharges from underlying permeable glacial deposits via peat pipes/conduits that terminate at the surface. (d) Drought conditions in northern peatlands driving downwelling of peat pore water towards the permeable esker ridges (modified from Reeve et al., 2009).

developed in response to 1) the topography changes and 2) the permeability contrast along the mineral sediment interface (Reeve et al., 2009). However, data from Sawtelle Heath indicate periods of continuous vertical discharge rates, modeled using VTP data, at an order of magnitude higher (tens of centimeters) than the lateral flow rates of peat pore water (Reeve et al., 2009). Additionally, relatively strong groundwater discharge rates are necessary to create observable temperature anomalies at land surface, otherwise downward conduction of land surface heat dominates (Hare et al., 2017). The persistent vertical groundwater discharge observed in the Sawtelle Heath VTP data during periods of minimal precipitation (recharge to the local glaciofluvial aquifer) indicates groundwater upwelling might operate in tandem with peat pore water flow cells (Fig. 10b). Notable precipitation events enhance the upwelling rates from the underlying glaciofluvial aquifer via preferential flow pathways, explaining the dominance of groundwater thermal expressions in pools during these periods and convergence of VTP temperature signals with depth (Fig. 10c); these periods of enhanced upwelling occurred when local precipitation exceeded 25 mm/d. Further, during extended dry periods when hydraulic heads in the local glaciofluvial aquifer fall below that of the peatland water table. downwelling to the esker ridges would occur as the permeable soils function as drains (Fig. 10d) as previously modeled by Reeve et al. (2009) and Bon et al. (2014).

We recognize that the pool complex present in Sawtelle Heath is not representative of more typical patterned pools, that are characterized by a dense clustering of multiple pools in one area, as often observed in northern peatlands. We find a strong correspondence between the pools and imaged underlying permeable glacial esker deposits whereas this was not the case for all patterned pools investigated by Comas et al. (2011). Additional imaging could help verify pipe structures to constrain the hydraulic connectivity between the pools and underlying glacial sediments. Data collected in this study challenge the generic ombrogenous model of peatland bogs, with localized groundwater upwelling influencing the hydrology of the system. The localized nature of such groundwater inputs highlights the importance of targeted hydrogeophysical methods to determine the ombrogenous versus geogenous state of hydrologic inputs to peatlands. Further, groundwater upwelling in and around peatland pools may impose unrecognized influences on carbon cycling in northern peatlands (Limpens et al., 2008). The rapid alterations to vertical flow could potentially enhance carbon ebullition during periods of upwelling and lead to enhanced degradation of the peat matrix. The water balance of northern peatland basins could be impacted by groundwater upwelling, with greater groundwater inputs during exceptionally wet climatic conditions suggested by the vertical upwelling measured in this study. Further, groundwater wells are often drilled in these glacial esker aquifers (Thompson et al., 2006), suggesting that over pumping from anthropogenic water use could drain northern peatland bogs in Maine, USA. Additional research could support the determination of the importance of groundwater seepage to the overall water balance of these northern peatlands.

5. CONCLUSION

Hydrogeophysical investigations provide evidence for groundwater originating in permeable glacial sediments below and adjacent to peat deposits sourcing peatland pools and other surface water features. Meteoric water naturally accumulates within the peatland and therefore the pools are unlikely to be composed of only groundwater from the local glacial aquifer. The deployment of thermal characterization methods provides unique insights into preferential groundwater flow influencing pools. Surveys conducted using GPR replicate the success of previous peatland studies through the identification of stratigraphy beneath organic sediments and the delineation of spatial distributions of glacial esker ridges hypothesized to drive groundwater upwelling. Zones feeding pools coincide with highly localized terminations of suspected peat piping, with some zones of matrix upwelling occurring in areas with

strong vertical upwelling flux. Vertical fluxes estimated for matrix seeps increase shortly after precipitation events, suggesting that local recharge overpressurizes the underlying glaciofluvial aquifer and enhances preferential flow through vertical peat piping.

Future hydrogeophysical investigations could focus on patterned pool systems found in northern peatlands, and possible links between groundwater connectivity and pool formation. Supporting ecological investigations could reveal how nutrient and thermal regimes associated with preferential seepage zones regulate vegetation patterns. Geophysical imaging of peat pipe geometries could help to constrain the hydrological connectivity between peat pipe upwelling zones and the underlying mineral soil stratigraphy in northern peatlands. Hydrology is inherently linked to carbon accumulation and release within peatland environments. Studying the impacts of groundwater upwelling could yield novel insights into localized processes controlling these greenhouse gases. Further exploration into the role of upwelling groundwater in peatland pools may lead to a paradigm shift in the understanding of the hydrology of northern peatlands.

CRediT authorship contribution statement

Henry E. Moore: Conceptualization, Data curation, Formal analysis, Investigation, Methodology, Supervision, Validation, Visualization, Roles/Writing – original draft, Writing – review & editing. Xavier Comas: Writing – review & editing, Validation, Supervision, Resources, Project administration, Methodology, Investigation, Funding acquisition, Data curation, Conceptualization. Martin A. Briggs: Writing – review & editing, Validation, Supervision, Resources, Methodology, Data curation, Conceptualization. Andrew S. Reeve: Writing – review & editing, Validation, Supervision, Resources, Project administration, Investigation, Funding acquisition, Conceptualization. Lee D. Slater: Writing – review & editing, Validation, Supervision, Resources, Project administration, Methodology, Investigation, Funding acquisition, Conceptualization.

Declaration of competing interest

The authors declare that they have no known competing financial interests or personal relationships that could have appeared to influence the work reported in this paper.

Data availability

Data have been made available publicly via the Hydroshare repository at: Moore, H., X. Comas, M. A. Briggs, A. S. Reeve, L. Slater (2024). Sawtelle Heath Supplementary Data, HydroShare, http://www.hydroshare.org/resource/e7a9e0482b654399998fa71fb5d209ab.

Acknowledgements

This material is based upon workfunded by the National Science Foundation under Grant No. EAR 2502004. The authors would like to thank Josh and Danny Wood of Baileyville, Maine for their field expertise and assistance with data collection. Any use of trade, firm, or product names is for descriptive purposes only and does not imply endorsement by the U.S. Government. M. Briggs time on this project was funded by the Toxic Substances Hydrology Program. A. Reeve was also supported by the Maine Agricultural and Forestry Experiment Station [Grant Number ME022208] during this project. We would also like to extend our appreciation to Khondaker Md. "Tutul" Nur Alam and Dr. Ashaki Rouff for their guidance with designing the ICP-OES workflow used for this research.

Appendix A. Supplementary data

Supplementary data to this article can be found online at https://doi.

org/10.1016/j.jhydrol.2024.131479.

References

- Baird, A.J., Comas, X., Slater, L.D., Belyea, L.R., Reeve, A.S., 2009. Understanding carbon cycling in northern peatlands: Recent developments and future prospects. Geophys. Monogr. Ser. 184, 1–3.
- Baker, M.A., Dahm, C.N., Valett, H.M., 2000. Chapter 11: Anoxia, Anaerobic Metabolism, and Biogeochemistry of the stream-water-Groundwater Interface. In: Jones, J.B., Mulholland, P.J. (Eds.), Streams and Ground Waters. Elsevier, pp. 260–280.
- Bendell-Young, L., 2003. Peatland Interstitial Water Chemistry in Relation to that of Surface Pools along a Peatland Mineral Gradient. Water Air Soil Pollut. 143, 363-375.
- Bon, C.E., Reeve, A.S., Slater, L., Comas, X., 2014. Using hydrologic measurements to investigate free-phase gas ebullition in a Maine peatland, USA. Hydrol. Earth Syst. Sci. 18, 953-965.
- Borns Jr., H.W., 1963. Preliminary report on the age and distribution of the late Pleistocene ice in north-central Maine. Am. J. Sci. 8, 738-740.
- Bourgault, M.A., Larocque, M., Garneau, M., 2019. How do hydrogeological setting and meteorological conditions influence water table depth and fluctuations in ombrotrophic peatlands?. Journal of Hydrology X, 4, 100032.Bragg, O. M., (2002). Hydrology of peat-forming wetlands in Scotland. Sci. Total Environ. 294, 111–129.
- Briggs, M.A., Lautz, L.K., McKenzie, J.M., Gordon, R.P., Hare, D.K., 2012. Using high-resolution distributed temperature sensing to quantify spatial and temporal variability in vertical hyporheic flux. Water Resour. Res. 48, W02527.
- Briggs, M.A., Lautz, L.K., Buckley, S.F., Lane, J.W., 2014. Practical limitations on the use of diurnal temperature signals to quantify groundwater upwelling. J. Hydrol. 519, 1739-1751.
- Briggs, M.A., Buckley, S.F., Bagtzoglou, A.C., Werkema, D.D., Lane, J.W., 2016. Actively heated high-resolution fiber-optic-distributed temperature sensing to quantify streambed flow dynamics in zones of strong groundwater upwelling. Water Resour. Res. 52, 5179-5194.
- Casas-Mulet, R., Pander, J., Ryu, D., Stewardson, M.J., Geist, J., 2020. Uncrewed Aerial Vehicle (UAV)-Based Thermal Infra-Red (TIR) and Optical Imagery Reveals Multi-Spatial Scale Controls of Cold-Water Areas Over a Groundwater-Dominated Riverscape. Front. Environ. Sci. 8, 64.
- Chanton, J.P., Bauer, J.E., Glaser, P.A., Siegel, D.I., Kelley, C.A., Tyler, S.C., Romanowicz, E.H., Lazrus, A., 1995. Radiocarbon evidence for the substrates supporting methane formation within northern Minnesota peatlands. Geochim. Cosmochim. Acta 59 (17), 3663–3668.
- Chen, X., Comas, X., Reeve, A., Slater, L., 2020. Evidence for glacial geological controls on the hydrology of Maine (USA) peatlands. Geology 48 (8), 771–776.
- Clymo, R.S., 1984. The Limits to Peat Bog Growth. Philos. Trans. R. Soc. Lond. B Biol. Sci. 303 (1117), 605–654.
- Comas, X., Slater, L.D., Reeve, A., 2004. Geophysical evidence for peat basin morphology and stratigraphic controls on vegetation observed in a Northern Peatland. J. Hydrol. 295. 173–184.
- Comas, X., Slater, L., Reeve, A., 2005. Stratigraphic controls on pool formation in a domed bog inferred from ground penetrating radar (GPR). J. Hydrol. 315 (1–4), 40–51.
- Comas, X., Slater, L., Reeve, A., 2007. In situ monitoring of free-phase gas accumulation and release in peatlands using ground penetrating radar (GPR). Geophys. Res. Lett. 34, L06402.
- Comas, X., Slater, L., Reeve, A.S., 2011. Pool patterning in a northern peatland: Geophysical evidence for the role of postglacial landforms. J. Hydrol. 399 (3–4), 173–184.
- Comas, X., Slater, L., Reeve, A., 2021. The Role of the Critical Zone Structure on the Hydrology and Pool Patterning of Boreal Peatlands. FastTIMES 26 (3).
- Espinoza-Quiñones, F.R., Módenes, A.N., De Pauli, A.R., Palácio, S.M., 2015. Analysis of Trace Elements in Groundwater Using ICP-OES and TXRF Techniques and Its Compliance with Brazilian Protection Standards. Water Air Soil Pollut. 226, 32.
- Ferlatte, M., Quillet, A., Larocque, M., Cloutier, V., Pellerin, S., Paniconi, C., 2015. Aquifer-peatland Connectivity in Southern Quebec (Canada). Hydrol. Process. 29 (11), 2600-2612.
- Giardino, J.R., Houser, C., 2015. Introduction to the Critical Zone. Developments in Earth Surface Processes 19, 1-13.
- Glaser, P.H., Siegel, D.I., Romanowicz, E.A., Shen, Y.P., 1997. Regional linkages between raised bogs and the climate groundwater, and landscape of north-western Minnesota. J. Ecol. 85, 3–16.
- $\label{eq:Global} Global, A., 2022. \ Aetha \ ThermoConverter \ (Version \ 1.3.14.0) \ [Computer Software].$ $Aetha \ Global. \ https://aetha.global/product/thermoconverter/.$
- Gordon, R.P., Lautz, L.K., Briggs, M.A., McKenzie, J.M., 2012. Automated calculation of vertical pore-water flux from field temperature time series using the VFLUX method and computer program. J. Hydrol. 420–421, 142–158.
- Groschen, G. E., Arnold, T. L., Morrow, W. S., and Warner, K. L., 2009. Occurrence and Distribution of Iron Manganese, and Selected Trace Elements in Ground Water in the Glacial Aquifer System of the Northern United States. U.S. Geological Survey Scientific Investigations Report 2009-5006, 89 p.
- Handcock, R.N., Torgensen, C.E., Cherkauer, K.A., Gillespie, A.R., Tockner, K., Faux, R. N., Tan, J., 2012. Thermal Infrared Remote Sensing of Water Temperature in Riverine Landscapes. In: Fluvial Remote Sensing for Science and Management. John Wiley & Sons Inc., pp. 85–113
- Hare, D.K., Boutt, D.F., Clement, W.P., Hatch, C.E., Davenport, G., Hackman, A., 2017. Hydrogeological controls on spatial patterns of groundwater discharge in peatlands. Hydrol. Earth Syst. Sci. 21 (12), 6031–6048.

- Harvey, M.C., Hare, D.K., Hackman, A., Davenport, G., Haynes, A.B., Helton, A., Briggs, M.A., 2019. Evaluation of stream and wetland restoration using UAS-based thermal infrared mapping. Water (switzerland) 11 (8).
- Hill, A.R., 2012. The impact of pipe flow in riparian peat deposits on nitrate transport and removal. Hydrol. Process. 26 (20), 3135–3146.
- Holden, J., Burt, T.P., 2002. Piping and pipeflow in a deep peat catchment. Catena 48 (3), 163–199.
- Holden, J., Burt, T.P., Vilas, M., 2002. Application of Ground-Penetrating Radar to the Identification of Subsurface Piping in Blanket Peat. Earth Surf. Proc. Land. 27, 235–249.
- Hribljan, J.A., Kane, E.S., Pypker, T.G., Chimner, R.A., 2014. The effect of long-term water table manipulations on dissolved organic carbon dynamics in a poor fen peatland. J. Geophys. Res. Biogeo. 119, 577-595.
- Hu, F.S., Davis, R.B., 1995. Postglacial development of a Maine bog and paleoenvironmental implications. Can. J. Bot. 73, 638–649.
- Integrated, M., 2009. OneWire Viewer. Retrieved from: https://www.maximintegrated.com/en/products/ibutton-one-wire/one-wire/software-tools/viewer.html.
- Irvine, D.J., Lautz, L.K., Briggs, M.A., Gordon, R.P., McKenzie, J.M., 2015. Experimental evaluation of the applicability of phase, amplitude, and combined methods to determine water flux and thermal diffusivity from temperature time series using VFLUX 2. J. Hydrol. 531 (3), 728-737.
- Irvine, D.J., Briggs, M.A., Lautz, L.K., Gordon, R.P., McKenzie, J.M., Cartwright, I., 2017. Using Diurnal Temperature Signals to Infer Vertical Groundwater-Surface Water Exchange. Groundwater 55 (1), 10–26.
- Kline, M., 2014. Peatland-Stream Hydrological and Biogeochemical Connectivity in the James Bay Lowland. The University of Western Ontario (Canada), Ontario.
- Le Maitre, D.C., Scott, D.F., Colvin, C., 1999. A review of information on interactions between vegetation and groundwater. Water SA 25 (2), 137–152.
- Limpens, J., Berendse, F., Blodau, C., Canadell, J.G., Freeman, C., Holden, J., Roulet, N., Rydin, H., Schaepman-Strub, G., 2008. Peatlands and the carbon cycle: from local processes to global implications – a synthesis. Biogeosciences 5 (2), 1379–1419.
- Lowry, C.S., Fratta, D., Andersen, M.P., 2009. Ground penetrating radar and spring formation in a groundwater dominated peat wetland. J. Hydrol. 373, 68-79.
- Ludman, A., and Hill, M., 1990. Bedrock Geology of the Calais 15' Quadrangle, Eastern Maine. Department of Conservation, Maine Geological Survey Open-File No. 90-27, 1-35
- Ludman, A., 1990. Bedrock Geology of the Big Lake 15' Quadrangle, Maine. Department of Conservation Maine Geological Survey, Open-File No. 90-26, 1-25.
- Maine Department of Agriculture, Conservation, & Forestry. 2021. Focus Areas of Statewide Ecological Significance Sawtelle Heath. Beginning with Habitat, 1-6.
- Maine Geological Survey, 2016. Maine LiDAR Project Footprint [Data File]. Retrieved from: State of Maine. https://www.maine.gov/geolib/catalog.html.
- Maine Geological Survey, 2017. Maine Surficial Geology 500K Marine Limit [Data File].

 Retrieved from: State of Maine, https://www.maine.gov/geolib/catalog.html.
- Maine Geological Survey, 2019. Maine Peat Resources [Data File]. Retrieved from: State of Maine, https://www.maine.gov/geolib/catalog.html.
- National Oceanic & Atmospheric Administration (NOAA), 2022. Record of Climatological Observations August 2022, Grand Lake Stream, Maine, US, Station: GRAND LAKE STREAM, ME US USC00173261. National Centers for Environmental Information. Retrieved from: https://www.ncei.noaa.gov/cdo-web/.
- National Oceanic & Atmospheric Administration (NOAA), 2022. Record of Climatological Observations October 2022, Grand Lake Stream, Maine, US, Station: GRAND LAKE STREAM, ME US USC00173261. National Centers for Environmental Information. Retrieved from: https://www.ncei.noaa.gov/cdo-web/.
- National Oceanic & Atmospheric Administration (NOAA), 2022. Record of Climatological Observations September 2022, Grand Lake Stream, Maine, US, Station: GRAND LAKE STREAM, ME US USC00173261. National Centers for Environmental Information. Retrieved from: https://www.ncei.noaa.gov/cdo-web/.
- Osberg, P.H., Hussey, I.I., A.M., and Boone, G.M., 1985. Bedrock Geologic Map of Maine, 1:500,000. Maine Geological Survey. Maine Department of Conservation, Augusta, MF.
- Penrose, R.A.F., 1893. The Chemical Relation of Iron and Manganese in Sedimentary Rocks. J. Geol. 1 (4), 356–370.
- Plattner, A.M., 2020. GPRpy: open-source ground-penetrating radar processing and visualization software. Leading Edge 39 (5), 332–337.
- QGIS.org, 2022. QGIS Geographic Information System. Retrieved from, QGIS Association http://www.qgis.org.
- Reeve, A.S., Siegel, D.I., Glaser, P.H., 2000. Simulating vertical flow in large peatlands. J. Hydrol. 227, 207–217.
- Reeve, A.S., Siegel, D.I., Glaser, P.H., 2001. Simulating dispersive mixing in large peatlands. J. Hydrol. 242 (1-2), 103-114.
- Reeve, A.S., Evensen, R., Glaser, P.H., Siegel, D.I., Rosenberry, D., 2006. Flow path oscillations in transient ground-water simulations of large peatland systems. J. Hydrol. 316 (1-4), 313-324.
- Reeve, A.S., Tyczka, Z.D., Comas, X., Slater, L.D., 2009. The Influence of Permeable Mineral Lenses on Peatland Hydrology. Am. Geophys. Union. Geophysical Monograph Series 184.
- Rossi, P.M., Ala-aho, P., Ronkanen, A.K., Kløve, B., 2012. Groundwater-surface water interaction between an esker aquifer and a drained fen. J. Hydrol. 432, 52–60.
- Rydin, H., Jeglum, J., Bennett, K., 2013. The Biology of Peatlands, 2e, second ed. Oxford University Press.
- Shreve, R.L., 1985. Esker characteristics in terms of glacier physics, Katahdin esker system. Maine. Geol. Soc. Am. Bull. 96, 639-646.
- Siegel, D.I., Glaser, P.H., 1987. Groundwater Flow in a Bog-Fen Complex, Lost River Peatland, Minnesota. J. Ecol. 75, 743–754.

- Slater, L., Reeve, A., 2002. Understanding peatland hydrology and stratigraphy using integrated electrical geophysics. Geophysics 67, 365–378.
- Cole, S.W., 1992. Supplemental hydrogeologic investigation. Rep., S.W. Cole Eng., Inc., Bangor, Maine, Orono Municipal Landfill, Tech.
- Teledyne, F.L.I.R., 2018. Teledyne FLIR Tools / FLIR Tools+ (Version 6.4). [Computer Software]. Teledyne FLIR.
- Theimer, B.D., Nobes, D.C., Warner, B.G., 1994. A study of the geoelectrical properties of peatlands and their influence on ground-penetrating radar surveying. Geophys. Prosp. 42, 179–209.
- Thompson, W. B., Borns, H. W., Jr., Brennan, T., and Dubois, M., 2006. Glacial and groundwater geology of the Rangeley-Stratton area, western Maine, in Gibson, D., Daly, J., and Reusch, D., eds., Guidebook for field trips in western Maine September 29th to October 1st, 2006: Farmington, ME, University of Maine at Farmington, guidebook for 98th annual New England Intercollegiate Geological Conference, p. 89-108.
- Trefethen, J.M., Harris, J.N., 1940. A fossiliferous esker-like deposit (Maine). Am. J. Sci 238 (6), 408–412.
- Waswa, G.W., Lorentz, S.A., 2019. Dynamics of groundwater flow and upwelling pressure heads at a wetland zone in a headwater catchment. Springer Nature Applied Sciences 1 (9).
- Weber, C.A., 1902. U'ber die Vegetation und Entstehung des Hochmoors von Augstumal im Memeldelta mit vergleichenden Ausblicken auf andere Hochmoore der Erde. Paul Parey, Berlin.
- Weber, C.A., 1908. Aufbau und Vegtationen der Moore Nord-deutschlands Englers. Bot. Jahrb. 40 (Suppl.), 29–34.
- West, D.P., Ludman, A., Lux, D.R., 1992. Silurian Age for the Pocomoonshine Gabbro-Diorite, Southeastern Maine and Its Regional Tectonic Implications. Am. J. Sci. 292, 253-273
- Woo, M.K., DiCenzo, P., 1988. Pipe flow in James Bay coastal wetlands. Can. J. Earth Sci. 25 (4), 625–629.